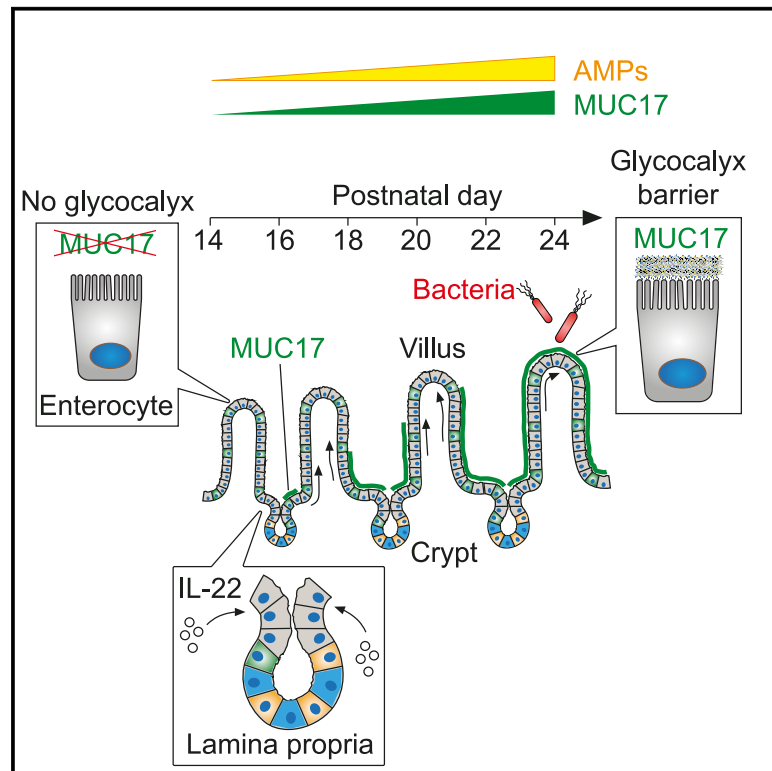# IL-22 promotes the formation of a MUC17 glycocalyx barrier in the postnatal small intestine during weaning

Graphical Abstract

Authors

Elena Layunta, Sofia Jäverfelt,
Brendan Dolan, Liisa Arike,
Thaher Pelaseyed

Correspondence

thaher.pelaseyed@medkem.gu.se

In Brief

Layunta et al. use a multi-omics approach to identify membrane mucin MUC17 as a major component of the glycocalyx covering enterocytes of the distal small intestine. IL-22 signaling during weaning upregulates MUC17 that guards enterocytes against exogenous luminal molecules and bacteria.

Highlights

- Multi-omics analysis identifies MUC17 as a major membrane mucin in ileum

- MUC17 localizes to apical glycocalyx covering enterocytic brush-border membranes

- IL-22 signaling during weaning upregulates MUC17 in enterocytes

- MUC17 guards enterocytes from exogenous molecules and bacteria

CelPress

Article

IL-22 promotes the formation of a MUC17 glycocalyx barrier in the postnatal small intestine during weaning

Elena Layunta,[1] Sofia Jäverfelt,[1] Brendan Dolan,[1] Liisa Arike,[1] and Thaher Pelaseyed[1,2,*]

[1]Department of Medical Biochemistry and Cell Biology, Institute of Biomedicine, University of Gothenburg, Box 440, 405 30 Gothenburg, Sweden
[2]Lead contact
*Correspondence: thaher.pelaseyed@medkem.gu.se
https://doi.org/10.1016/j.celrep.2021.108757

SUMMARY

The intestine is under constant exposure to chemicals, antigens, and microorganisms from the external environment. Apical aspects of transporting epithelial cells (enterocytes) form a brush-border membrane (BBM), shaped by packed microvilli coated with a dense glycocalyx. We present evidence showing that the glycocalyx forms an epithelial barrier that prevents exogenous molecules and live bacteria from gaining access to BBM. We use a multi-omics approach to investigate the function and regulation of membrane mucins exposed on the BBM during postnatal development of the mouse small intestine. Muc17 is identified as a major membrane mucin in the glycocalyx that is specifically upregulated by IL-22 as part of an epithelial defense repertoire during weaning. High levels of IL-22 at time of weaning reprogram neonatal postmitotic progenitor enterocytes to differentiate into Muc17-expressing enterocytes, as found in the adult intestine during homeostasis. Our findings propose a role for Muc17 in epithelial barrier function in the small intestine.

INTRODUCTION

The gastrointestinal tract constitutes the largest contact area between the human body and the outside world (Helander and Fändriks, 2014). The small intestinal epithelium is organized in folds of crypts and protruding villi that are lined by a single layer of rapidly self-renewing intestinal epithelial cells (IECs) (Clevers, 2013). Enterocytes, the most abundant IEC type, maintain tissue homeostasis by performing vital functions such as ion transport, nutrient absorption, and transmission of information from the gut lumen to specialized immune cells in underlying lamina propria (Cheng and Leblond, 1974). Apical aspects of differentiated enterocytes display a typical brush-border membrane (BBM), shaped by an array of tightly packed microvilli (Granger and Baker, 1950), which are coated with a dense layer of membrane-bound glycoproteins and glycolipids, collectively termed glycocalyx (Cheng and Leblond, 1974). Despite the fact that the enterocytic glycocalyx was described over half a century ago (Ito, 1969), its function remains unknown.

Membrane mucins have been extensively studied in the context of cancer development, but their function at the interface of host enterocytes and the microbe-rich intestinal lumen remains undefined. Membrane mucin MUC17 is expressed in the BBM of enterocytes throughout the human small intestine and colon (Malmberg et al., 2008; Pelaseyed et al., 2013a). MUC17 is a 4,493-amino-acid-long single-pass transmembrane protein with an extracellular fragment containing recurring tandem repeats, rich in proline, threonine, and serine (PTS) residues

(Gum et al., 2002). PTS-rich sequences are frequently O-glycosylated in the Golgi apparatus, forming an extended mucin domain (Olson et al., 2005; Roth, 1987). The cytoplasmic tail (CT) domain of MUC17 contains a conserved postsynaptic density protein (PSD95), Drosophila disc large tumor suppressor (DlgA), and Zonula occludens-1 protein (ZO-1) (PDZ) binding motif that allows for interaction with PDZ-containing protein 1 (PDZK1). In Pdzk1-deficient mice, murine Muc17 is absent from the BBM of duodenal enterocytes (Malmberg et al., 2008).

Enterocytic proliferation, differentiation, and apoptosis is governed by intrinsic tissue-specific programs (Middendorp et al., 2014). Cytokine production in lamina propria is associated with both maintenance of epithelial homeostasis and pathologic conditions such as tissue damage and inflammation (Gronke et al., 2019; Takashima et al., 2019). Furthermore, a complex consortium of luminal bacteria produces microbial molecules alongside metabolites from fermentation of dietary and host-derived carbohydrates that regulate IECs and immune cells (Camp et al., 2014). Luminal microbiota undergoes dramatic changes during the postnatal period; directly after birth, the intestine is colonized by maternal bacteria that are later replaced during suckling-weaning transition by an expanding and diverse microbial community adapted to plant-based carbohydrates in a solid diet (Al Nabhani et al., 2019). While it is widely recognized that weaning is associated with maturation of neonatal innate immunity (Menard et al., 2008), there is a knowledge gap concerning the formation and function of the enterocyte-specific glycocalyx throughout postnatal development.

In the current work, we used mouse ileum as a model for investigating postnatal regulation and function of membrane mucins. Our investigation reveals that Muc17 is the major membrane mucin localized to the BBM of enterocytes. Muc17 is specifically upregulated during weaning by interleukin (IL)-22, a homeostatic cytokine that promotes expression of a wide range of intestinal defense genes. *In vivo* cell tracking revealed that upregulation of Muc17 by IL-22 does not involve the whole epithelium but is restricted to non-proliferative progenitor enterocytes in intestinal crypts, which mature and replace the neonatal epithelium. Finally, by quantifying glycocalyx permeability, we demonstrate that Muc17 protects enterocytes against exogenous molecules and live bacteria residing in the gut lumen. In conclusion, our results argue that Muc17 is intimately associated with defense programs that meet the functional demands of suckling-weaning transition in the distal small intestine.

RESULTS

Enterocytic glycocalyx is formed during weaning and functions as a barrier against exogenous molecules and bacteria

The intestine is home to trillions of microbes that produce a diverse collection of exogenous molecules. Bacterial load reaches its maximum in the distal colon, where an impermeable inner mucus layer separates microbes dwelling in an outer mucus layer from the host epithelium (Johansson et al., 2008). In the small intestine, a considerably lower number of bacteria reside within an unattached, permeable mucus layer (Ermund et al., 2013), which allows bacteria and bacterial molecules to interact with enterocytes. Electron microscopic investigation of ileal enterocytes in weaned mice (postnatal day 28, P28) showed that the BBM along villus protrusions was coated with a dense glycocalyx (Figure 1A, right panel; Figure S1A, right panel). However, this dense glycocalyx was absent from the enterocytic BBM in ileum of pre-weaned mice (P15) (Figure 1A, left panel; Figure S1A, left panel). Consequently, we hypothesized that the glycocalyx functions as a cell-attached barrier that is established during suckling-weaning transition. To test our hypothesis, we designed a glycocalyx permeability assay in which whole-mount ileum was extensively flushed to remove secreted mucus, thus allowing for assessment of glycocalyx barrier function. Fixed whole-mount tissue was stained with CellMask to label BBM prior to incubation with fluorophore-conjugated anionic Dextran 2,000 kDa that mimics net negative surface charge of intestinal bacteria. Dextran 2,000 kDa was effectively blocked from diffusion into the BBM region (Figure 1B, top panels; Figure S1B, top panel), suggesting that glycocalyx on BBM in weaned mice is impermeable to large molecules with ≥ 1 μm radius, like Dextran 2,000 KDa (Neu et al., 2008). In contrast, Dextran 2,000 kDa penetrated into the BBM of fixed whole-mount tissue of P14 mice, as validated by quantification of Dextran 2,000 kDa distribution in relation to CellMask (Figure 1B, bottom panels; Figure S1B, bottom panel), suggesting that lack of glycocalyx leaves BBM of pre-weaned mice exposed to exogenous molecules. Next, we expanded our glycocalyx permeability assay to time-lapse imaging of live GFP-expressing *E. coli* (*E. coli*[GFP]) added to whole-mount ileum. At P24, *E. coli*[GFP] were segregated

from the BBM (Figure 1C top panels; Video S1), while *E. coli*[GFP] made frequent direct contact with the BBM at P14 (Figure 1C, bottom panels; Video S2). Tracking of *E. coli*[GFP] in time-lapse images revealed a significant increase of colocalization between *E. coli*[GFP] tracks and CellMask-stained BBM at P14 compared to P24 (Figure 1C; Figure S1C). In support of the barrier function of glycocalyx, electron micrographs of P24 ileum showed that the glycocalyx separated luminal bacteria from microvilli of enterocytes (Figure 1D). In summary, the glycocalyx that coats distal tips of microvilli in BBM is established during weaning and functions as a protective barrier against bacteria and bacteria-sized exogenous molecules.

MUC17 is a major membrane mucin on brush-border membranes in human and mouse ileum

We have previously shown that Muc17, a SEA-type membrane mucin (Figure 2A), is expressed in BBM of murine small intestinal enterocytes (Malmberg et al., 2008; Pelaseyed et al., 2013a). Here, we sought to establish a comprehensive profile of membrane mucin expression in mouse ileum. Bulk RNA sequencing (RNA-seq) analysis of whole mouse ileum revealed high expression of *Muc13* and *Muc17*, while *Muc1* and *Muc4* displayed significantly lower transcript numbers (Figure 2B). Of note, *Muc17* is the ortholog of human *MUC17* but is annotated as *Muc3* in mouse genome and proteome databases (Gum et al., 2002; Malmberg et al., 2006). Transcriptomic data were supported by proteomic analysis of purified IECs, which identified Muc13 and Muc17 as the dominating membrane mucins in mouse ileum (Figure 2C). Omics data were empirically validated using immunostaining that showed prominent staining of Muc13 in BBM of murine ileal enterocytes positioned along the length of villi and in crypt bottoms (Figure 2D, left panel). Muc17 was also strongly expressed along villi while staining in crypts was weaker (Figure 2D, right panel). In analogy with mouse ileum, MUC13 and MUC17 were readily expressed in the enterocytic BBM in human ileum (Figure 2E). Importantly, in both mouse (Figure 2F) and human ileum (Figure 2G), MUC17 was expressed at distal tips of microvilli where we observed glycocalyx formation during weaning (Figure 1A).

Muc17 expression increases during suckling-weaning transition

Based on the finding that Muc13 and Muc17 are major membrane mucins in the lumen-facing BBM, we sought to investigate membrane mucin expression during the course of postnatal development from birth to post-weaning marked by postnatal day 24 (P24). As expected, Muc17 displayed a typical BBM staining in post-weaned P24 mice (Figure 3A, right panel). Strikingly, in P14 mice only a faint intracellular Muc17 staining was observed in enterocytes, and Muc17 was completely absent from the BBM (Figure 3A, left panel). Proteomic analysis of purified IECs and immunoblot of whole ileal tissues showed negligible Muc17 expression at P14 and high Muc17 expression at P24 (Figures 3B and 3C). Notably, Muc13 localized to BBMs in both P14 and P24 mice (Figure 3D). Establishment and maintenance of microvilli requires Ezrin that transiently crosslinks cytoskeletal F-actin to plasma membranes and actin bundlers such as Villin (Vil-1) (Pelaseyed and Bretscher, 2018; Pelaseyed
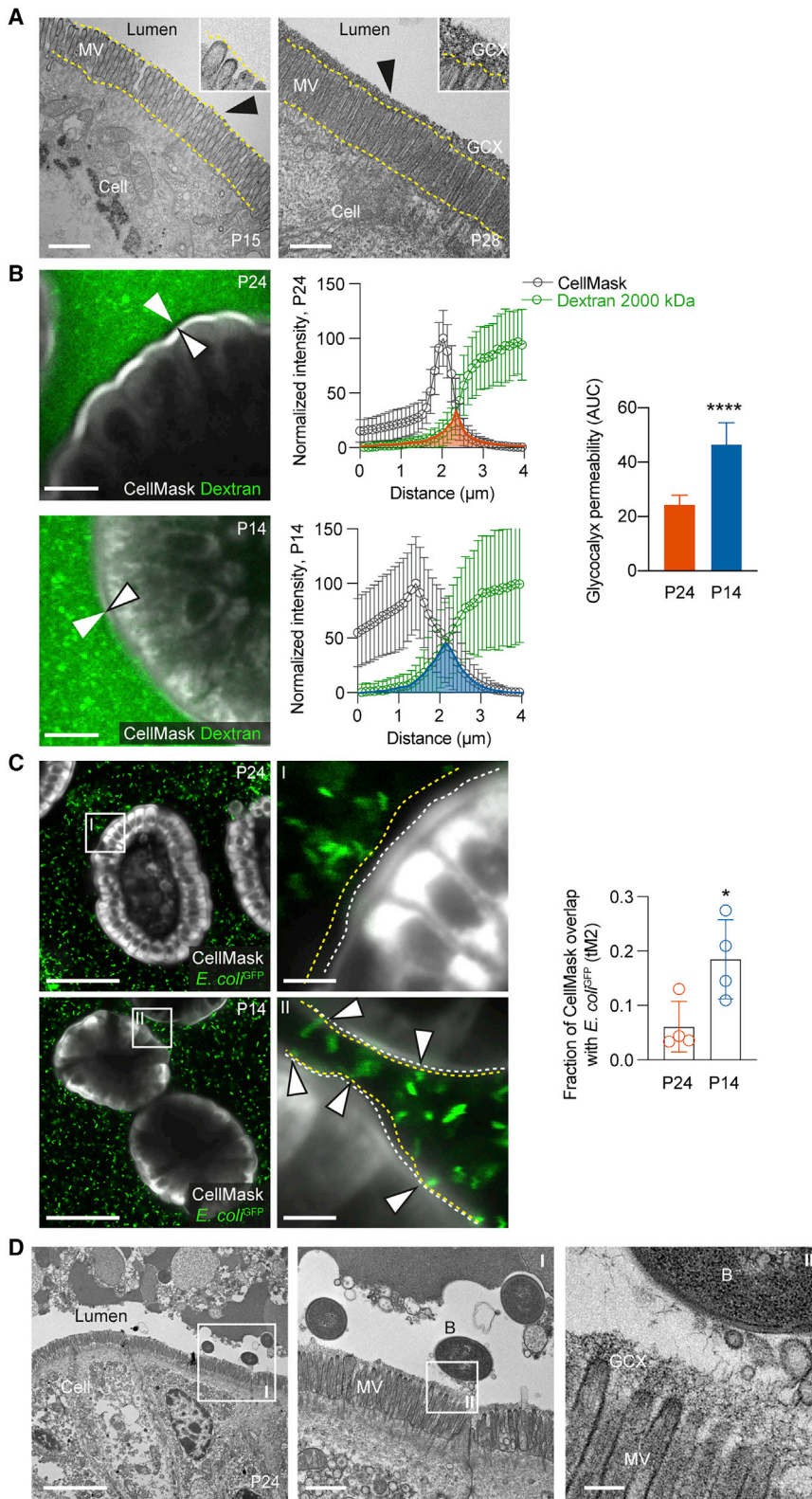
Figure 1. Enterocytic glycocalyx established during weaning forms a barrier against live bacteria and exogenous molecules

(A) Electron micrographs of enterocytic BBM in P15 (left panel) and P28 (right panel) ileum. Black arrows point to position of glycocalyx (GCX) on microvilli (MV). Scale bars 500 nm. See also Figure S1A.

(B) Assessment of glycocalyx permeability in fixed whole-mount ileum of P24 (top panels) and P14 mice (bottom panels). Separation of luminal Dextran 2,000 kDa (green) from CellMask plasma membrane stain (gray) is marked with white arrows. Line profiles show separation of Dextran 2,000 kDa (green) from CellMask (black) in P24 and P14 ileum, as quantified by area under the curve (AUC) for each age group. Scale bar 10 μm. n = 3 lines per image, 3 images per animal, and 3 animals per age group. ****p ≤ 0.0001 as determined using two-tailed unpaired t test with Welch's correction. Data are represented as mean ± SD. See also Figure S1B.

(C) Assessment of glycocalyx permeability in fixed whole-mount ileum shows separation of *E. coli*[GFP] (green) from CellMask plasma membrane stain (gray) at P24 (top panels) and P14 (bottom panels). White arrows indicate overlap between *E. coli*[GFP] and CellMask in P14 ileum, as quantified by thresholded Manders coefficient (tM2) for each age group. Scale bar 50 μm and 10 μm in corresponding insets. n = 26 regions per villus, 3 villi per animal, and 4 animals per age group. *p ≤ 0.05 as determined using two-tailed unpaired t test with Welch's correction. Data are represented as mean ± SD. See also Figure S1C and Videos S1 and S2.

(D) Glycocalyx (GCX) on microvilli (MV) separates bacteria (B) from villus enterocytes in P28 ileum. Scale bar 5 μm. Scale bar in inset I 1 μm. Scale bar in inset II 200 nm.

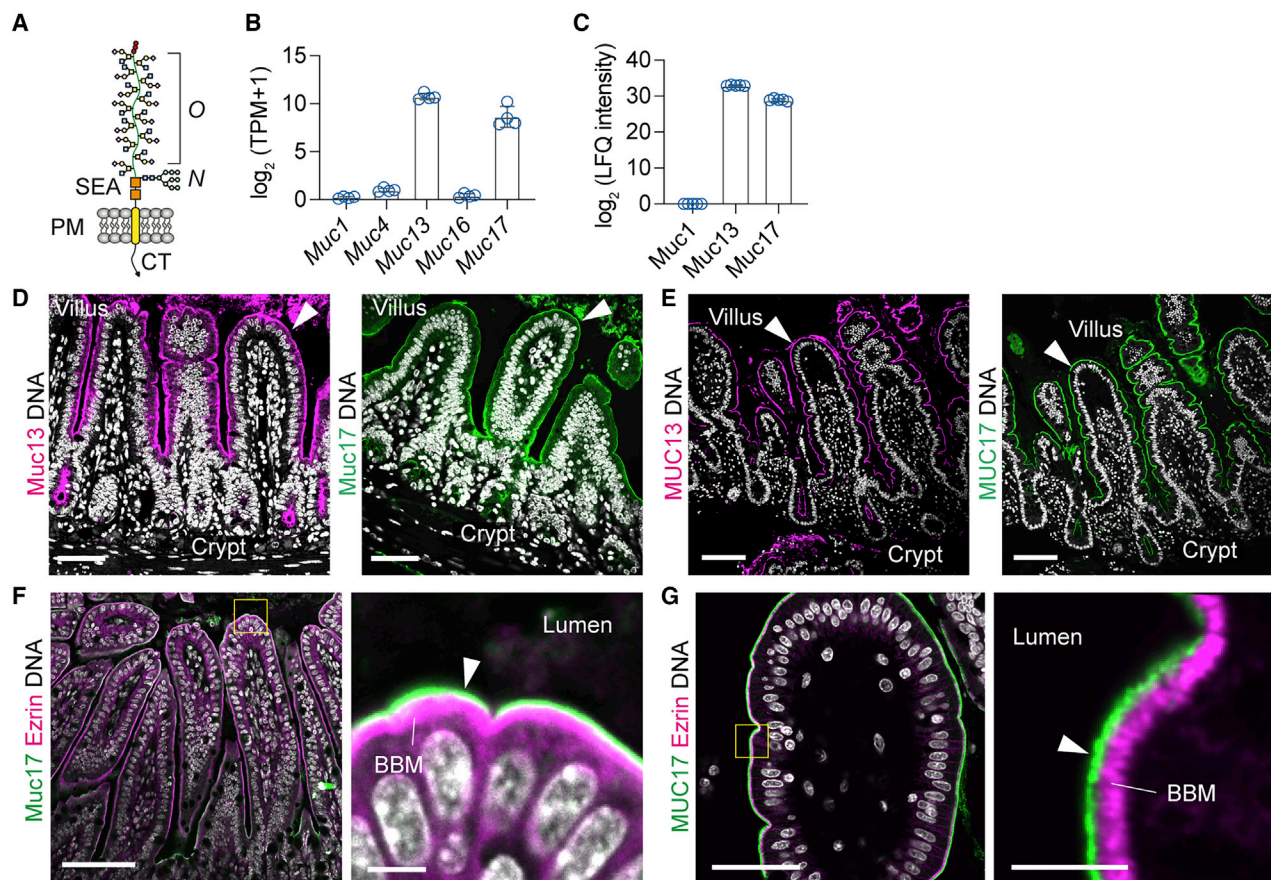**Figure 2. Muc13 and Muc17 are major membrane mucins in mouse ileum**

(A) Schematic representation of MUC17. CT, cytoplasmic tail; PM, plasma membrane; SEA, Sperm protein, Enterokinase and Agrin domain; O, O-glycans; N, N-glycans.

(B) Number of transcripts per million (TPM) of membrane mucins in bulk RNA-seq of whole ileal tissue from adult mice. n = 4. Data are represented as mean ± SD.

(C) Label-free quantification of membrane mucins in IECs isolated from mouse ileum using proteomic analysis. n = 5. Data are represented as mean ± SD.

(D) Confocal sections of mouse ileum stained for Muc13 (magenta), Muc17 (green), and DNA (gray). White arrows point to BBM. Scale bars 50 μm.

(E) Confocal sections of human ileum stained for MUC13 (magenta), MUC17 (green), and DNA (gray). White arrows point to BBM. Scale bars 100 μm.

(F) White arrow points at Muc17 (green) covering BBM stained with Ezrin (magenta) in a section of mouse ileum. DNA stain is in gray. Scale bar 50 μm and 5 μm in the corresponding inset.

(G) White arrow points at MUC17 (green) covering BBM stained with Ezrin (magenta) in a section of human ileum. DNA stain is in gray. Scale bar 50 μm and 5 μm in corresponding inset.

et al., 2017). Enterocytes of the neonatal small intestine perform non-selective endocytosis of luminal solutes, nutrients, and macromolecules, termed macropinocytosis (Arévalo Sureda et al., 2016). In analogy with Muc13, both Ezrin and Vil-1 resided in BBM independent of age, thus suggesting that absence of Muc17 from cell surfaces was not caused by bulk internalization of apical membrane proteins as a result of macropinocytosis (Figure 3D). In a detailed assessment of postnatal membrane mucin kinetics, Muc17 expression increased at P19 after which Muc17 emerged on BBMs and culminated at P24 coinciding with increased *Muc17* transcript numbers during suckling-weaning transition (P19-P24) (Figure 3E). We also observed an increase in Muc17 expression in duodenum at time of weaning, suggesting that Muc17 upregulation associated with weaning is not limited to ileum but occurs throughout the small intestine (Figures S2A–S2D). Combined Alcian blue periodic acid-Schiff

(AB-PAS) staining of P24 ileum revealed intense staining of neutral and acidic glycans covering villus BBM, while AB-PAS staining was weak in BBMs at P14 (Figure 3F), correlating with absence of Muc17 from BBM at this age. We concluded that Muc17 is a major glycoprotein component of the enterocytic apical glycocalyx that is specifically upregulated in the mouse small intestine during weaning.

Upregulation of Muc17 is synchronous with the formation of postnatal intestinal defenses

We asked whether the abrupt upregulation of Muc17 at P19-P24 was part of a wider tissue-specific program executed during weaning. We carried out bulk RNA-seq analysis of whole ileal mucosal RNA and proteomics analysis of purified IECs from P14 and P24 mice. Unsupervised hierarchical clustering revealed distinct networks of genes and proteins upregulated
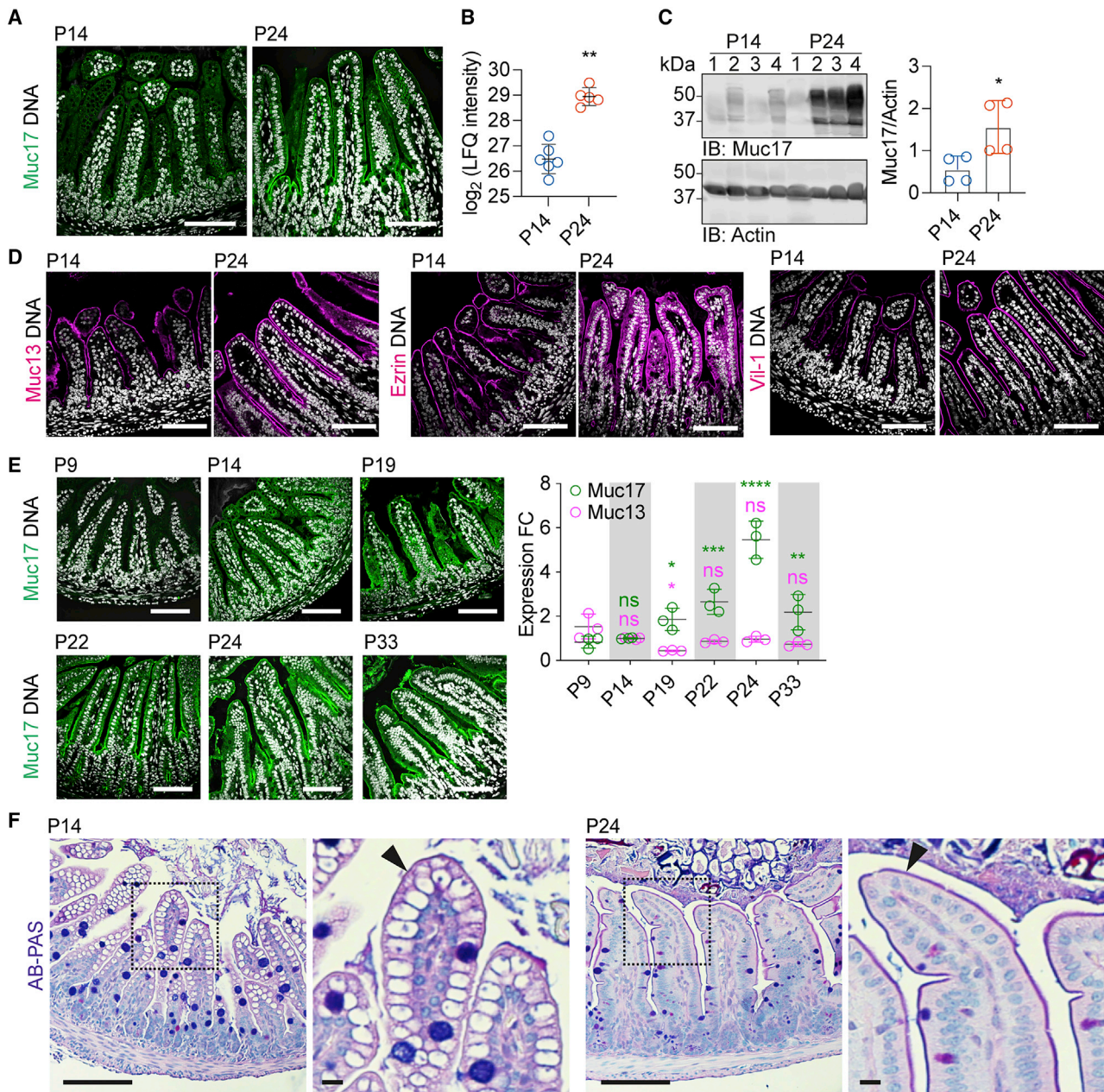
Figure 3. Muc17 expression in ileum increases during weaning

(A) Confocal sections of mouse ileum at P14 and P24 stained for Muc17 (green) and DNA (gray). Scale bars 50 μm.

(B) Label-free quantification of Muc17 in proteomic analysis of purified ileal IECs from P14 and P24 mice. n = 6 for P14 group, n = 5 for P24 group. **p ≤ 0.01 as determined using two-tailed unpaired t test followed by Mann-Whitney test. Data are represented as mean ± SD.

(C) Immunoblot analysis of Muc17 in lysates of mouse ileum from P14 and P24 mice. Loading control is Actin. n = 4 for each group. *p ≤ 0.05 as determined using two-tailed unpaired t test followed by Mann-Whitney's test. Data are represented as mean ± SD.

(D) Confocal sections of mouse ileum at P14 and P24 stained for Muc13, Ezrin, and Vil-1 in magenta and DNA (gray). Scale bars 50 μm.

(E) Confocal sections of ileum from P9-P33 mice stained for Muc17 (green) and DNA (gray). Scale bars 50 μm. Quantitative RT-PCR of *Muc13* (magenta) and *Muc17* (green) transcripts in ileum of P9-P33 mice. n = 3 for each group. ns p > 0.05, *p ≤ 0.05, **p ≤ 0.01, ***p ≤ 0.001, ****p ≤ 0.0001 as determined using two-way ANOVA, corrected for multiple comparison within each gene group using Dunnett's test. Data are represented as mean ± SD.

(F) AB-PAS staining on BBM (black arrows) in ileal sections from of P14 and P24 ileum. Scale bars 50 and 10 μm in corresponding insets.
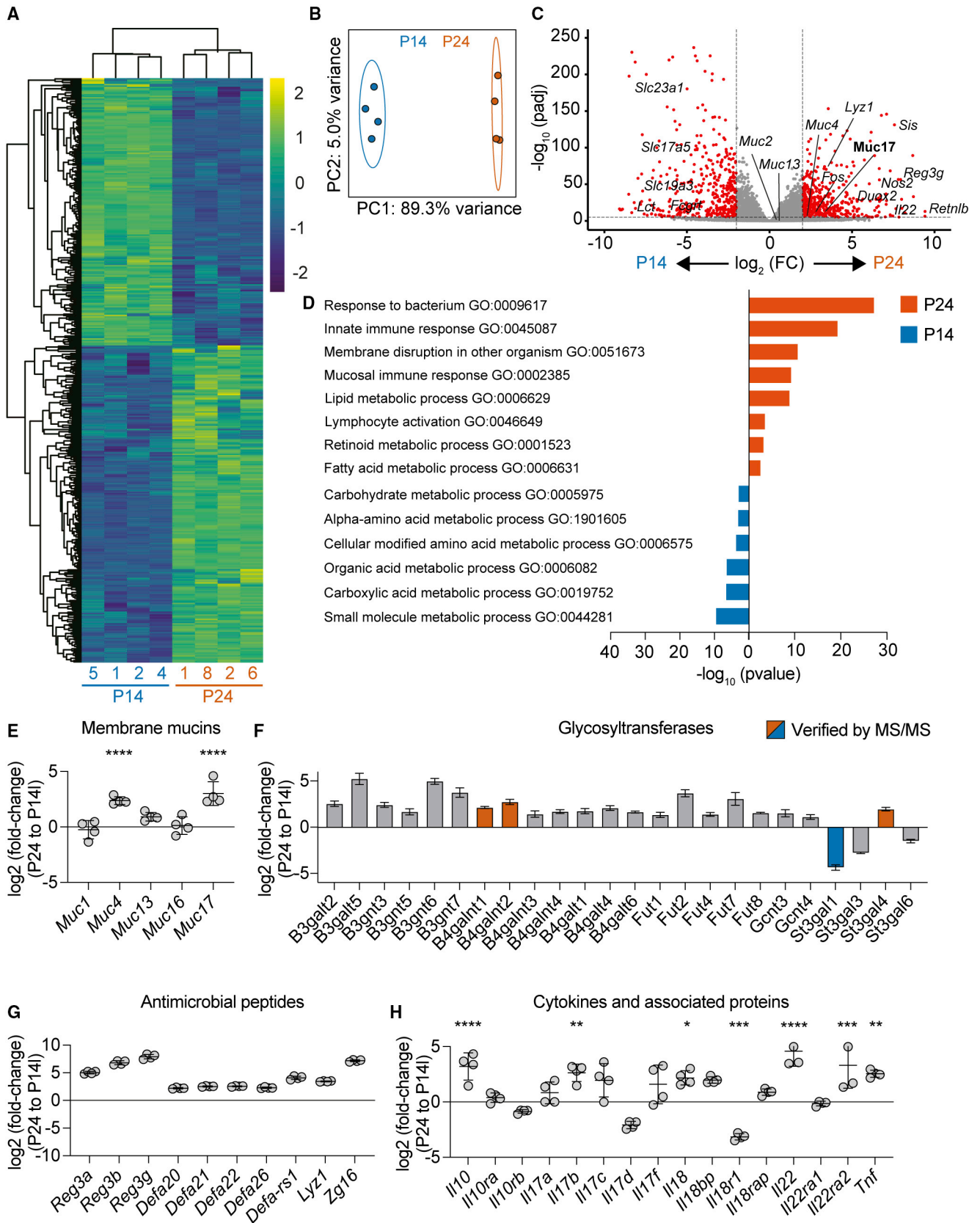
(legend on next page)

following weaning (Figures 4A and 4B; Figures S3A and S3B). Upregulated genes in P24 animals included genes involved in mucosal innate immune response, such as antimicrobial proteins (bactericidal C-lectins Reg family, CC and CXC motif chemokines, antibacterial defensins, and Zg16) and proteins that give rise to reactive nitrogen and oxygen species (*Duox1*, *Duox2*, *Nos2*, and *Nox1*) (Figures 4C and 4D). Brush-border enzymes, such as sucrase-isomaltase (*Sis*) required for digestion of dietary carbohydrates were also upregulated in P24 animals (Figure 4C). We observed upregulation of genes involved in epithelial cell division, differentiation, and proliferation (*Fos*, *Olfm4*, and to a lesser extent *Klf4* and *Klf6*) (Figure 4C; Figure S3C). Moreover, retinoic acid sensing (*Gprc5a*) and retinol metabolism (*Aldh1a7*, *Cyp1a1*, and *Rdh9*) were upregulated (Figure 4D), alongside bile acid uptake (*Slc10a2*) and metabolism (*Cyp2c55*, *Pla2g2f*, *Ces2c*, and *Cyp4f14*) (Tables S1 and S2). Expectedly, genes enriched in P14 ileum performed functions associated with the preweaning neonatal period, such as milk oligosaccharide digestion and uptake (lactase *Lct*, lysosomal neuraminidase *Neu1* and sialidase transporter *Slc17a5*), vitamin uptake (*Slc19a3* and *Slc23a1*), and import of protective immunoglobulins from milk to serum (*Fcgrt*) (Figure 4C; Tables S1 and S2). Specifically, we observed upregulation of Muc17 gene and protein expression at P24, while Muc13 expression remained unchanged during the suckling-weaning transition (Figures 4C and 4E; Figure S3C). Membrane mucins carry *N*- and *O*-glycans, and we observed upregulation of glycosyltransferases that generate extended *O*-glycan structures in P24 ileum (Figure 4F; Figure S3D). Antimicrobial peptides (AMPs) such as *Reg3b*, *Reg3g*, *Defa20*, *Defa21*, *Defa22*, and *Lyz1* were significantly upregulated as part of the formation of mucosal defenses following weaning (Figure 4G; Figure S3E). Mucosal defense genes expressed by IECs are governed by coordinated cytokine signals originating from the epithelium and underlying lamina propria. We observed upregulation of cytokines *Il10*, *Il17b*, *Il18*, *Il22*, and tumor necrosis factor α (*Tnfα*) at P24 (Figure 4H). In conclusion, weaning is associated with a significant structural remodeling of the epithelium alongside rewiring of nutrient absorption pathways and protective functions in response to changes in diet and microbiota. Among these significant changes, we identified specific upregulation of membrane mucin Muc17 (Tables S1 and S2).

IL-22 signaling associated with weaning upregulates Muc17 expression

Intestinal maturation after birth is regulated by tissue-intrinsic programs and external signals conveyed from the gut lumen to host IECs and immune cells. Our RNA-seq data identified several cytokines that were upregulated during weaning. IL-10 is a central anti-inflammatory cytokine secreted by IECs and a wide variety of immune cells, and perturbations in IL-10 signaling have been implicated in inflammatory bowel disease (IBD) (Kole and Maloy, 2014; Kühn et al., 1993). IL-22 promotes several genes involved in enforcing intestinal defense function, including *Reg3b* and *Reg3g* (Zheng et al., 2008). IECs express receptor complexes for IL-10 (Il10ra/Il10rb) and IL-22 (Il22ra1/Il10rb) but not the IL-18 receptor complex (Il18r1/Il18rap) (Hanash et al., 2012; Kominsky et al., 2014; Mizuno et al., 2014). Consequently, we asked whether mouse recombinant (r)Il10 and rIl22 could induce *Muc17* expression in purified IECs from ileum of P14 and P24 mice. Expression of *Muc17* and *Reg3g* increased upon stimulation of P14 IECs with rIl22 but not with rIl10 (Figure 5A), whereas neither cytokine was able to promote *Muc17* and *Reg3g* expression in P24 IECs (Figure 5B), indicating that IL-22 signaling promotes *Muc17* expression primarily before the suckling-weaning transition. Next, we interrogated epithelial-only 3D organoid cultures derived from ileum of an adult mouse with a conventional microbiota (Sato et al., 2009). Ileal organoids consisted predominantly of enterocytes interspersed with Muc2-expressing goblet cells, recapitulating *in vivo* epithelial cell organization (Figure S4A). Organoids treated with rIl22 for 4 and 16 h showed significant increase in *Muc17* transcripts compared to untreated cultures (Figure 5C). Of note, under sterile conditions, untreated organoids expressed significantly less *Muc17* transcripts compared to both neonatal P14 and postweaning P24 ileum (Figure 5D), suggesting that external signals from gut microbiota may regulate *Muc17* expression. Our bulk RNA-seq data showed significantly higher Toll-like receptor (*Tlr*) 1 and *Tlr3* transcripts at P24 compared to P14, while *Tlr5* transcript numbers decreased and *Tlr4* expression remained

---

Figure 4. Transcriptome of ileum after weaning reveals upregulation of *Muc17*, *Il22*, and defense genes

(A) Unbiased hierarchical clustering of bulk RNA-seq analysis of whole ileal tissues from P24 compared to P14 mice. The top 400 differentially expressed genes with adjusted p (padj) < 0.01 are displayed. n = 4 for each group. See also Figure S3A.

(B) Principal-component analysis shows dissimilarities between individual samples belonging to P14 (blue) and P24 (red) groups. n = 4 for each group. See also Figure S3B.

(C) Volcano plot showing fold change of gene expression in P24 compared to P14 ileum. n = 4 for each group. Genes with significantly different expression (fold change $\geq$ 2, padj < 0.01) are highlighted in red. Specific genes are labeled with gene names. See also Figure S3C.

(D) Gene ontology analysis shows significantly upregulated biological processes in P14 (blue) and P24 (red) groups, respectively.

(E) Fold change of transcripts of membrane mucins detected in bulk RNA-seq analysis of whole ileal tissues from P24 compared to P14 mice. n = 4 for each group. ****p $\leq$ 0.0001 as determined using 2-way ANOVA followed by Sidak's multiple comparison test. Data are represented as mean ± SD.

(F) Fold change of glycosyltransferases detected in bulk RNA-seq analysis of whole ileal tissue from P24 compared to P14 mice. Expression data confirmed by proteomic analysis are represented by red or blue bars. n = 4 for each group. Data are represented as mean ± SD. See also Figure S3D.

(G) Fold change of transcripts of significantly upregulated antimicrobial peptides detected in bulk RNA-seq analysis of whole ileal tissue from P24 compared to P14 mice. n = 4 for each group. Statistical analysis was performed using 2-way ANOVA followed by Sidak's multiple comparison test. Data are represented as mean ± SD. See also Figure S3E.

(H) Fold change of transcripts of cytokines and cytokine-associated proteins detected in bulk RNA-seq analysis of whole ileal tissue from P24 compared to P14 mice. n = 4 for each group. *p $\leq$ 0.05, **p $\leq$ 0.01, ***p $\leq$ 0.001, ****p $\leq$ 0.0001 as determined using 2-way ANOVA followed by Sidak's multiple comparison test. Data are represented as mean ± SD.
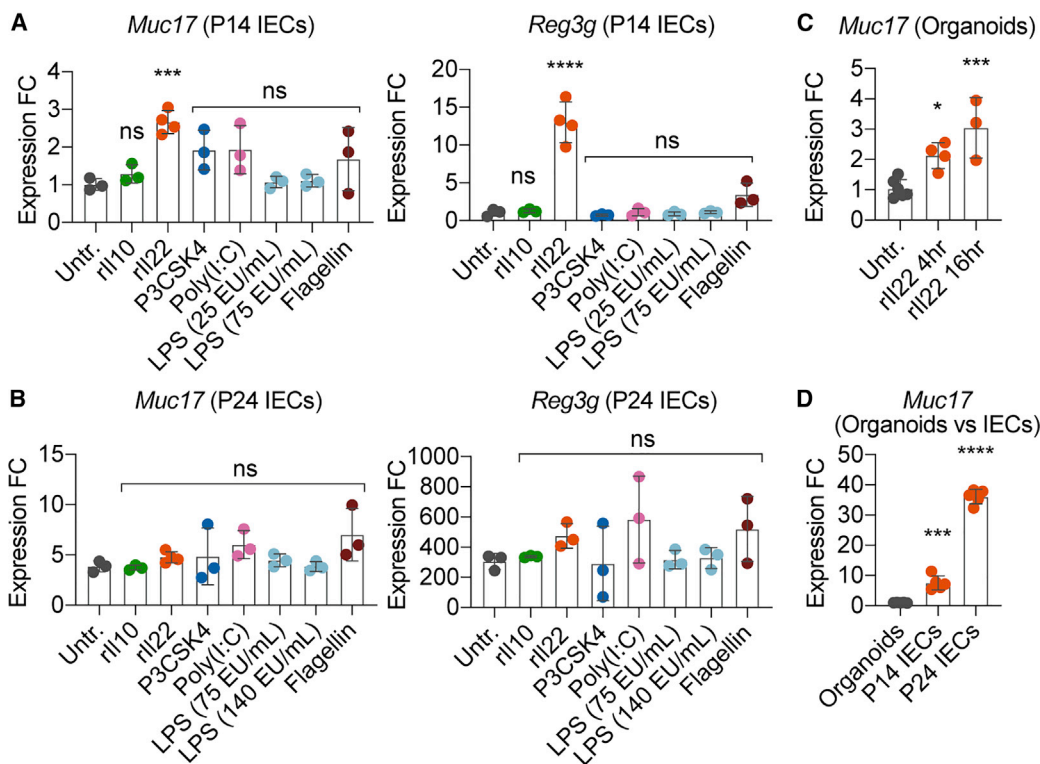
Figure 5. IL-22 upregulates *Muc17* expression in isolated ileal IECs and organoids

(A) Normalized expression fold change of *Muc17* and *Reg3g* in stimulated IECs isolated from P14 ileum. n = 4 for rIl22, n = 3 for all other conditions. ns p > 0.05, **p ≤ 0.01, ****p ≤ 0.0001 as determined using ordinary one-way ANOVA followed by Dunnett's multiple comparison test. Data are represented as mean ± SD. See also Figure S4C.

(B) Normalized expression fold change of *Muc17* and *Reg3g* in stimulated IECs isolated from P24 mice. n = 4 for rIl22, n = 3 for all other conditions. ns p > 0.05 as determined using ordinary one-way ANOVA followed by Dunnett's multiple comparison test. Data are represented as mean ± SD. See also Figure S4C.

(C) Normalized expression fold change of *Muc17* in ileal organoids after stimulation with rIl22. n = 6 for Untreated, n = 4 for rIl22 4 h, n = 3 for rIl22 16 h. *p ≤ 0.05, ***p ≤ 0.001 as determined using ordinary one-way ANOVA followed by Dunnett's multiple comparison test. Data are represented as mean ± SD. See also Figure S4A.

(D) Normalized expression fold change of *Muc17* in ileal organoids compared to IECs isolated from P14 and P24 ileum. n = 5. ***p ≤ 0.001, ***p ≤ 0.0001 as determined using ordinary one-way ANOVA followed by Dunnett's multiple comparison test. Data are represented as mean ± SD.

unchanged after weaning (Figure S4B). Physiological concentration of TLR4 ligand LPS in mouse ileum was 22.2 ± 9.5 EU/mL at P14 and 62.8 ± 41.0 EU/mL at P24 (Figure S4C). However, neither LPS at these physiological concentrations, Pam3CSK4 (TLR2 ligand), Poly(I:C) (TLR3 ligand), or Flagellin (TLR5 ligand) upregulated *Muc17* gene expression as quantified by qRT-PCR (Figures 5A and 5B). Moreover, the TLR ligands did not upregulate *Reg3g* in P14 and P24 ileal IECs (Figures 5A and 5B). In total, our findings suggest that IL-22 is the primary driver of *Muc17* expression in neonatal mouse ileum before weaning.

In vivo modeling of IL-22-induced Muc17 expression

Muc17 kinetics throughout postnatal development of ileum shows that Muc17 is upregulated between P19 and P24 (Figure 3E), perfectly coinciding with elevated *Il22* transcript levels during weaning (Figure 6A). We modeled postnatal IL-22 signaling *in vivo* by administering two single doses of rIl22 or PBS (vehicle) in 24-h intervals to P14 animals that exhibit inherently low ileal *Il22* gene expression (Figures 6A and 6B). Bulk RNA-seq of whole ileum of rIl22- or PBS-treated P16 animals re-

vealed that, while transcriptomic profiles of P14 and P16+PBS samples were similar, they collectively diverged from P24 samples. By contrast, P16+rIl22 samples were different from both P14 and P16+PBS groups and displayed a shift toward P24 (Figure 6C). We identified 75 upregulated IL-22-dependent genes in P16+rIl22 group, of which 50 genes were also significantly upregulated during weaning (P24 versus P14) (Figure S5A; Table S3). A third of these upregulated genes belonged to biological processes associated with defenses against gut bacteria (GO term response to bacterium, GO:0009617) and exhibited a strong correlation (r^2 = 0.483) with gene counterparts differentially expressed post- versus preweaning (Figure S5B; Table S3). Specifically, AMPs (*Reg3b* and *Reg3g*) and genes involved in production of reactive oxygen and reactive nitrogen species (*Nos2* and *Duox2*) were upregulated in response to rIl22 (Figure 6D). Targeted qRT-PCR detected significantly higher numbers of *Muc17* transcripts in whole ileal mucosal RNA upon treatment with rIl22 compared to vehicle control (Figure 6E). Glycosyltransferases that generate extended glycan structures during weaning were also upregulated by rIl22 (Figure 6F).

A *Il22*

B

C

D

E *Muc17*

F Glycosyltransferases

G *Muc17*

H Muc17 (BBM)
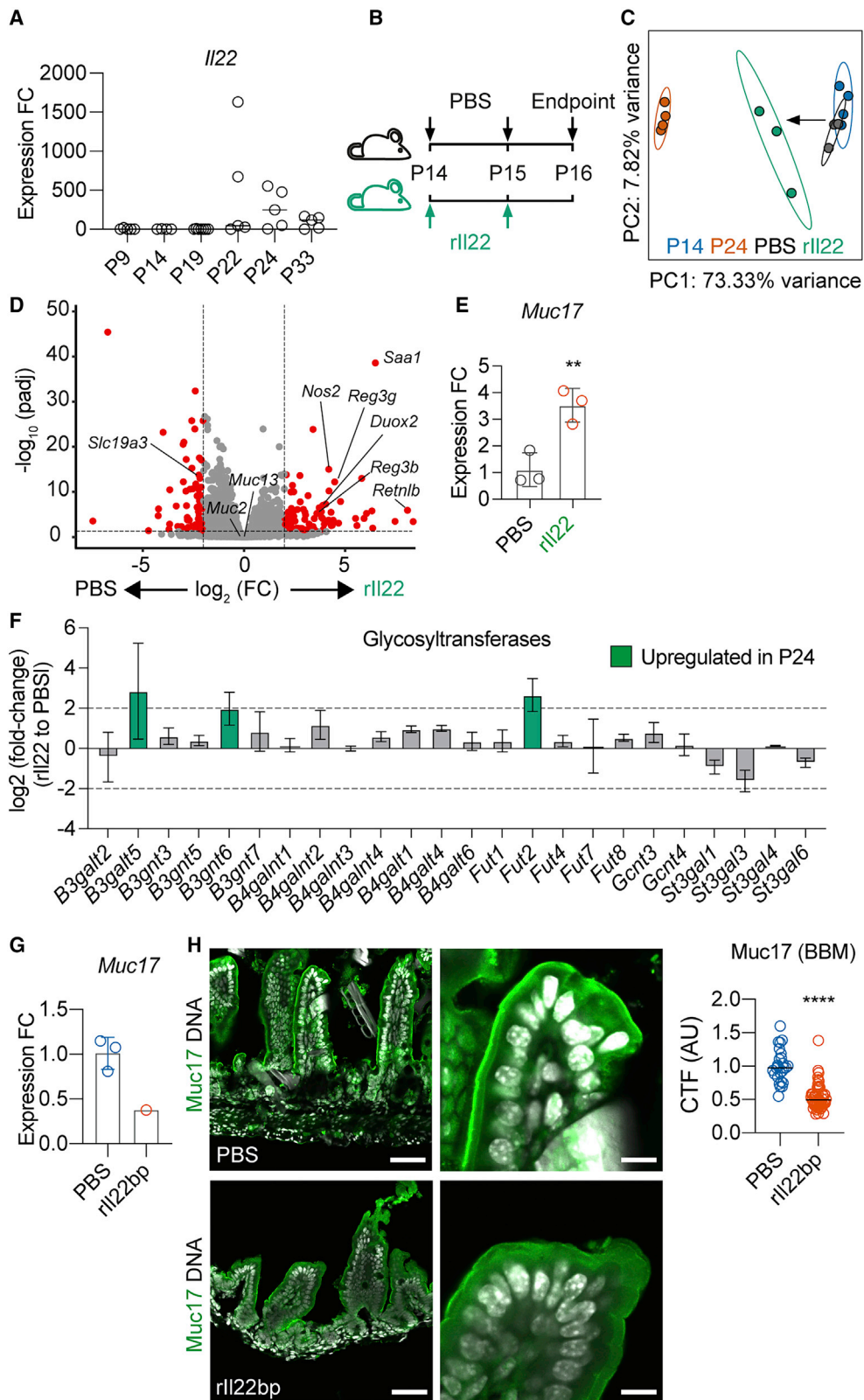
(legend on next page)

IL-22 binding protein (Il22bp or Il22ra2) is a soluble inhibitory IL-22 receptor with higher affinity for IL-22 than epithelial Il22ra1 receptor subunit (Wolk et al., 2007). In order to determine whether upregulation of Muc17 during weaning required IL-22, we produced pure recombinant mouse Il22bp (rIl22bp) (Figures S5C and S5D) and performed intraperitoneal injections with rIl22bp or PBS every second day from P14 to P18. At P20, *Muc17* gene expression was downregulated in presence of rIl22bp compared to PBS (Figure 6G). Semiquantitative analysis revealed significantly less Muc17 protein expression in BBM after rIl22bp compared to PBS treatment (Figure 6H), suggesting that IL-22 promotes upregulation of Muc17 in neonates approaching weaning age. In conclusion, we have identified an IL-22-dependent gene signature responsible for a postnatal intestinal defense program, of which membrane mucin Muc17 is an integral component (Table S3).

IL-22 primes postmitotic progenitor enterocytes to express Muc17

Next, we investigated the spatial expression of Muc17 in ileal sections of P16 mice injected with rIl22 or PBS at P14. We observed weak intracellular Muc17 expression in P16 ileum treated with PBS (Figure 7A). In rIl22-treated P16 ileum, Muc17 was expressed in BBM of IECs in the villus bottom (Figure 7A), suggesting that rIl22 signals locally to IECs within the intestinal crypt and lower half of villus rather than triggering a global upregulation of Muc17 within the entire epithelial cell layer. Consequently, we sought to determine the spatiotemporal expression of Muc17 in response to rIl22 treatment *in vivo*. To this end, we used 5-ethynyl-2′-deoxyuridine (EdU) pulse-chase assay to timestamp enterocytes in P14 mice upon rIl22 injection, followed by tracing of EdU$^+$ and Muc17$^+$ cells during 48 h after injection. Proliferating IECs within crypts had incorporated EdU 2 h after rIl22+EdU injection, but these cells did not express Muc17 in response to rIl22 at this time (Figure 7B, left panels). 24 h post-rIl22 injection (P15), tracked EdU$^+$ IECs were migrating upward within crypts, and Muc17 was expressed in BBM of EdU$^+$ cells and up to 3.2 ± 1.9 cells in front of EdU$^+$ cells (Figure 7B, mid panels). These forerunner Muc17$^+$ cells were also observed 2.5 ± 2.0 cells in front of EdU$^+$ IECs 48 h after injection (P16) (Figure 7B, right panels), suggesting that forerunner Muc17$^+$ IECs were non-proliferative, postmitotic progenitor enterocytes at the time of rIl22+EdU injection at P14. IECs in front of Muc17$^+$

forerunner cells that had differentiated further than progenitor enterocytes at the time of the rIl22+EdU pulse did not express Muc17, indicative of a narrow and defined spatial and temporal window during which non-proliferative progenitor enterocytes are receptive to IL-22 signaling. Our interpretation was supported by robust Il22ra1 expression in the top part of intestinal crypts and weaker staining in the stem cell compartment in crypt bases and villus region in P14 ileum (Figure 7C; Figure S6).

To further validate our *in vivo* modeling of IL-22-mediated Muc17 expression in P14 ileum, we investigated spatiotemporal distribution of Muc17 under steady-state conditions. P16 mice were injected with EdU, and ileal sections were prepared 2, 24, 48, 72, and 96 h after EdU injection. 2 h after injection (P16), proliferative cells in crypts were labeled with EdU, but Muc17 expression was negligible (Figure 7D). At P17 (24 h after injection), EdU$^+$ cells had started to migrate out of crypts, preceded by Muc17$^+$enterocytes. By 96 h after EdU injection (P20), EdU$^+$ IECs had reached the top of villi, and each villus was entirely covered with Muc17$^+$ enterocytes. We conclude that IL-22 primes postmitotic progenitor enterocytes to express Muc17. Primed Muc17$^+$ enterocytes leave intestinal crypts, migrate toward villus tips, and ultimately populate the whole epithelial monolayer by replacing neonatal Muc17$^-$ enterocytes.

DISCUSSION

The function and regulation of the glycocalyx covering small intestinal enterocytes is understudied. We applied a multi-omics approach to show that Muc17 is a major protein component of the glycocalyx established on enterocytes as part of a homeostatic intestinal defense repertoire at time of weaning. Elevated levels of IL-22 cytokine in lamina propria instruct postmitotic enterocytes in intestinal crypts to supersede neonatal epithelium with Muc17-expressing enterocytes through baseline cell turnover. Finally, our investigation unveils that the Muc17-based glycocalyx is a cell-attached barrier that protects enterocytes against bacterial attachment.

Membrane mucins are expressed at epithelial surfaces throughout the body; however, owing to a lack of reagents and genetic animal models, their function is grossly understudied (Pelaseyed and Hansson, 2020). In this study, we focused on membrane mucin expression in mouse ileum under homeostatic conditions, where we identified Muc13 and Muc17 on BBM of

Figure 6. *In vivo* modeling of IL-22 signaling upregulates Muc17 and defense genes

(A) Normalized expression fold change of *Il22* in ileum of P9-P33 mice. n = 5.

(B) Mice were administered rIl22 or PBS by intraperitoneal injection at P14 and P15. Ileal tissues were collected at P16.

(C) Principal component analysis of dissimilarities between transcriptomes of P14 (blue, n = 4), P16+PBS (black, n = 3), P16+rIl22 group (green, n = 3), and P24 (red, n = 4) groups.

(D) Volcano plot showing fold change of gene expression in PBS- versus rIl22-treated P16 mice. Genes with significantly different expression between the two groups (fold change ≥2, padj < 0.01) are highlighted in red. Specific genes are labeled with gene names. n = 3 for each group. See also Figure S5.

(E) Normalized expression fold change of *Muc17* in whole ileum of PBS- and rIl22-treated P16 mice. n = 3. **p ≤ 0.01 as determined using two-tailed unpaired t test followed by Mann-Whitney test. Data are represented as mean ± SD.

(F) Fold change of glycosyltransferases detected in bulk RNA-seq analysis of whole ileal tissue from P16+rIL22 compared to P16+PBS mice. Upregulated genes that were also upregulated in P24 mice are represented by green bars. n = 3 for each group. Data are represented as mean ± SD.

(G) Normalized expression fold change of *Muc17* in mouse ileum isolated from PBS- and rIl22bp-treated P20 mice. n = 3 for PBS, n = 1 for rIl22bp.

(H) Confocal sections of ileum from PBS- and rIl22bp-treated P20 mice stained for Muc17 (green) and DNA (gray). Scale bar 50 μm and 10 μm in insets. Semiquantitative analysis of Muc17 expression in BBM after PBS compared to rIl22bp treatment. n = 26 regions of interest for PBS. n = 52 regions of interest for rIl22bp. ****p ≤ 0.0001 as determined using two-tailed unpaired t test followed by Mann-Whitney test.
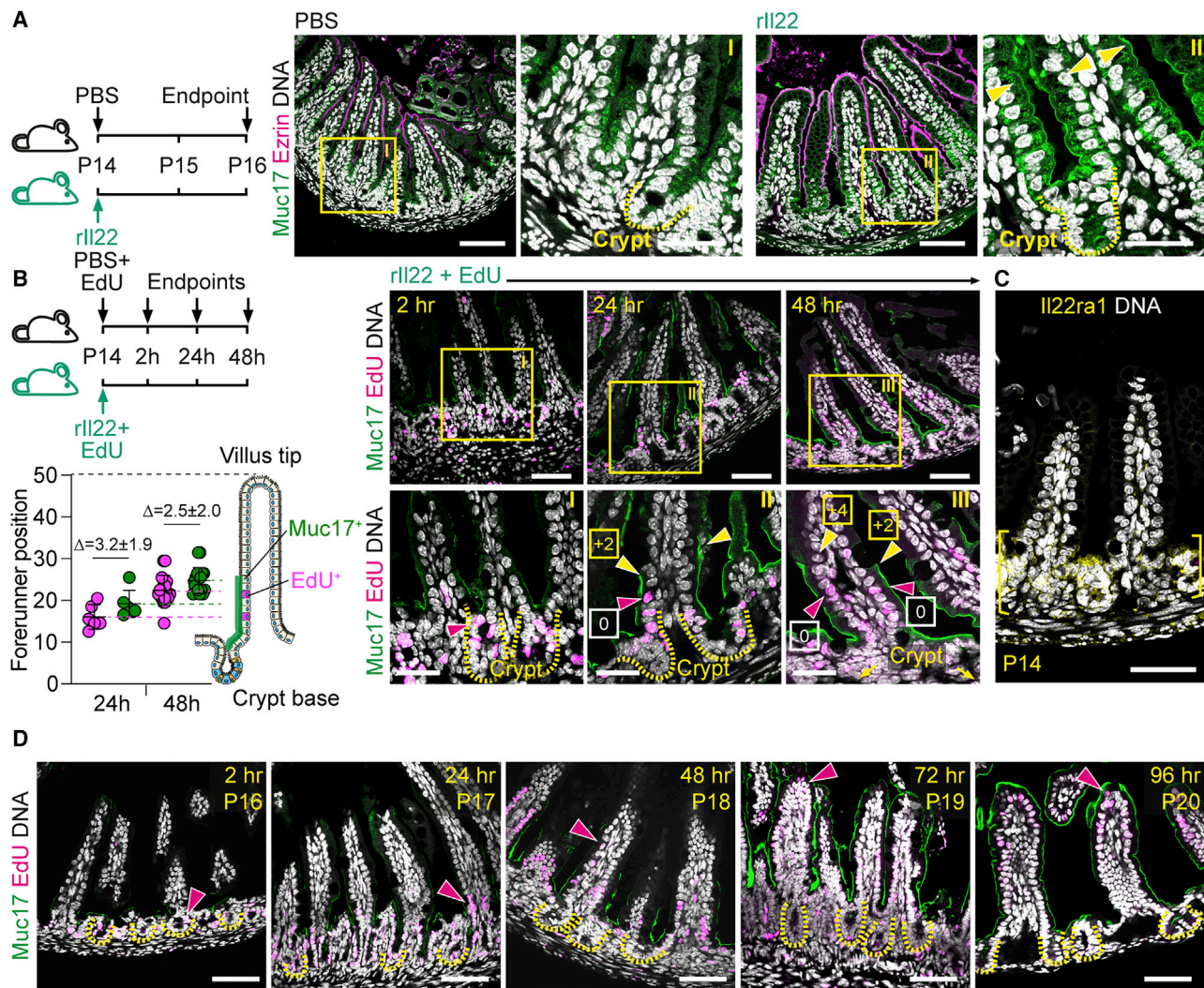
Figure 7. IL-22 primes postmitotic progenitor enterocytes to express Muc17

(A) Mice were administered rIl22 or PBS by i.p. injection at P14, and ileal tissues were collected for immunohistochemical analysis at P16. Ileal sections were stained for Muc17 (green), Ezrin (magenta), and DNA (gray). Scale bars 50 μm and 25 μm in corresponding insets, marked by roman numerals.

(B) Mice were administered rIl22 and EdU at P14. Ileal tissues were collected for immunohistochemical analysis 2, 24, and 48 h post-injection. Ileal sections were stained for Muc17 (green), EdU (magenta), and DNA (gray). Boxed numbers indicate forerunner Muc17^{+} enterocyte position (yellow arrows) in relation to EdU[+] IEC position (magenta arrows). Scale bars 50 μm and 25 μm in corresponding insets, marked by roman numerals. Data are represented as mean ± SD.

(C) Confocal sections of P14 ileum stained for Il22ra1 (yellow) and DNA (gray). Yellow brackets indicate the intestinal crypt region. Scale bars 50 μm. See also Figure S6.

(D) Mice were intraperitoneally injected with EdU at P16. Ileal tissues were collected for immunohistochemical analysis 2 , 24 (corresponding to P17), 48 (P18), 72 (P19), and 96 h (P20) post-injection. Ileal sections were stained for Muc17 (green), EdU (magenta), and DNA (gray). Arrows in magenta point to forerunner EdU^{+} cells in each villus. Scale bars 50 μm.

enterocytes. Muc13 and Muc17 are SEA-type membrane mucins, in which the extracellular subunit containing a mucin domain is non-covalently attached to the membrane-attached subunit at a Sperm protein, Enterokinase and Agrin (SEA) domain. The SEA domain is autocatalytically cleaved during in endoplasmic reticulum and unfolds when mechanical forces are applied to the mature membrane mucin (Macao et al., 2006; Pelaseyed et al., 2013b). The recent identification of two phosphorylation sites in human MUC17 CT suggests that phosphorylation may regulate MUC17 trafficking and function in yet-unidentified intracellular

signaling pathways (Schneider et al., 2019). Cholinergic stimulation of duodenal epithelium, a common outcome of bacterial infection, results in removal of MUC17 from enterocytic BBMs (Pelaseyed et al., 2013a). A portion of MUC17 is internalized in this process; however, membrane mucin shedding has not been excluded. Our current study reveals that Muc17 is differentially expressed along the mouse small intestine (duodenum and ileum) during postnatal development. Muc17 expression in neonatal mice is negligible, followed by a dramatic increase in Muc17 expression as neonates reach weaning age. AB-PAS staining

and electron microscopy confirmed presence of a glycocalyx at P24 that was strikingly absent from BBM at P14, indicative of an age-dependent correlation between Muc17 expression and formation of glycocalyx that covers enterocytes.

The suckling-weaning transition is a critical event during the life of mammals, hallmarked by the removal of maternal milk in favor of a solid diet. However, very few studies offer a comprehensive transcriptomic and proteomic profile of the small intestine during this developmental milestone. During weaning, the intestinal epithelium is remodeled for uptake of dietary plant-based carbohydrates and maintenance of homeostasis in a luminal environment shaped by expansion of a diverse community of adult-like microbes (Bäckhed et al., 2015; Koenig et al., 2011). Our study shows that epithelial programs executed during weaning include host defense genes, as previously reported (Cash, 2006; Al Nabhani et al., 2019). Alongside these defense genes, we identified membrane mucin Muc17, indicative of its role in innate immunity during intestinal development.

Cells within the intestinal epithelium react to external and intrinsic signals from the lumen and underlying lamina propria. Our exploration of pre- and post-weaning cytokine profiles identified elevated IL-22 expression at weaning. IL-22 is mainly produced by RAR-related orphan receptor (ROR)γt-expressing ILC3 (group 3 innate lymphoid cells) and binds the heteromeric epithelial-specific Il22ra1/Il10rb receptor complex (Cella et al., 2019; Hanash et al., 2012; Sawa et al., 2010; Vonarbourg et al., 2010). Several other studies have implicated IL-22 in promoting epithelial defense genes such as *Reg3b* and *Reg3g* (Price et al., 2018; Sonnenberg et al., 2012; Zheng et al., 2008). Our *in vitro* studies in purified IECs suggest that IL-22 is the main driver of Muc17 expression in neonatal ileum and excludes TLR-mediated sensing of microbial molecules by IECs as a route for sustained Muc17 expression. This neonatal receptivity for IL-22 corroborates the role of IL-22 in promoting epithelial defenses during weaning (Savage et al., 2017), which is likely suppressed by adaptive CD4+ T cells after weaning (Mao et al., 2018). Moreover, our *in vivo* modeling of IL-22 signaling to the epithelium recapitulated upregulation of genes that participate in epithelial response to bacteria, correlating with enforcement of epithelial defenses during weaning. The distinct spatiotemporal expression pattern of Muc17 in response to IL-22 prior to weaning as manifested in Muc17+ enterocytes originating from intestinal crypts is explained by expression of epithelial Il22ra1 receptor in upper crypts (Hanash et al., 2012). Consequently, when IL-22 levels increase during weaning, enterocytes embedded in this crypt region become primed to express Muc17 and ultimately replace neonatal Muc17⁻ enterocytes through basal cell turnover. A question that remains to be addressed is the identity of intrinsic and extrinsic signals that maintain Muc17 expression after weaning and throughout adulthood.

Microbial metabolism of dietary tryptophan generates indole derivatives that act as ligands for aryl hydrocarbon receptors that induce IL-22 production in immune cells (Lamas et al., 2016). Microbiota also orchestrates IL-22 production by regulating RORγt-dependent maturation of innate lymphocytes (Satoh-Takayama et al., 2008). Moreover, gut bacteria dictate the capacity of IECs to process dietary vitamin A to retinoic acid that regulates IL-22 production (Grizotte-Lake et al., 2018).

Importantly, signaling components downstream of epithelial Il22ra1 receptor, including Janus kinase 2 (JAK2), tyrosine kinase 2 (TYK2), and STAT3, have been implicated in IBD (Jostins et al., 2012; Silverberg et al., 2009), shedding light on the concerted function of IL-22-dependent defense programs in upholding intestinal homeostasis.

The production of mucus and AMPs, together with continuous peristalsis, prevents gut bacteria from colonizing the small intestinal epithelium. When these defenses fail, our findings suggest that Muc17 in the glycocalyx acts as a barrier that prevents bacteria from accessing the enterocytic BBM. Glycocalyx barrier function is likely determined by the extent of glycosylation as well as length and identity of glycan chains present on Muc17. Glycocalyx permeability assays showed that the glycocalyx effectively excluded anionic Dextran and live *E. coli* from BBM, suggesting that acidic glycans contribute to a negatively charged glycocalyx that repels lipopolysaccharide (LPS) and lipoteichoic acid (LTA) on Gram-negative and Gram-positive bacteria, respectively. We identified upregulation of several glycosyltransferases during weaning and sialyltransferase St3Gal4 is downregulated in germ-free mice (Arike et al., 2017, 2020), suggesting a role for bacteria in regulating membrane mucin glycosylation and glycocalyx barrier properties.

It is widely recognized that a key role of IL-22 in mucosal defenses is to promote epithelial cell regeneration and production of antimicrobial peptides. In the current study, we used comprehensive transcriptomics and proteomics to demonstrate that IL-22 supports Muc17 expression in enterocytes during a defined time window between birth and weaning. Our study suggests that IL-22 levels in lamina propria and epithelial receptor Il22ra1 expression in postmitotic progenitor enterocytes dictate the spatiotemporal dynamics of Muc17 in the developing ileum. Finally, we show that Muc17 constitutes a key component of the enterocytic glycocalyx barrier that protects enterocytes against luminal bacteria and molecules. In summary, we present Muc17 as a previously uncharacterized epithelial barrier component that protects enterocytes in response to functional demands of diet and microbiota in the small intestine after weaning.

STAR★METHODS

Detailed methods are provided in the online version of this paper and include the following:

- KEY RESOURCES TABLE
- RESOURCE AVAILABILITY
  - Lead contact
  - Materials availability
  - Data and code availability
- EXPERIMENTAL MODEL AND SUBJECT DETAILS
  - Human subjects
  - Mice
  - Mouse ileal organoids
  - Cell lines
  - Bacteria
- METHOD DETAILS
  - Determination of physiological concentration of LPS in mouse ileum

- ○ Stimulation of organoids and intestinal epithelial cells
- ○ *In vivo* treatment of mice with Il22 and 5-Ethynyl-2′-de-oxyuridine (EdU)
- ○ Production of recombinant IL-22 binding protein and intraperitoneal injection
- ○ Tissue and organoid fixation, immunostain, AB-PAS stain and microscopy
- ○ Semiquantitative image analysis
- ○ *Ex vivo* glycocalyx permeability assay
- ○ Electron microscopy
- ○ Electrophoresis and western blot
- ○ Quantitative RT-PCR
- ○ Bulk RNA-sequencing
- ○ Protein extraction and digestion for mass spectrometry
- ○ Liquid Chromatography-MS/MS
- ○ MS data analysis
- ● QUANTIFICATION AND STATISTICAL ANALYSIS

AUTHOR CONTRIBUTIONS

Conceptualization, E.L. and T.P.; methodology, E.L., S.J., B.D., L.A., and T.P.; investigation, E.L., S.J., B.D., L.A., and T.P.; writing – original draft, E.L. and T.P.; writing – review & editing, E.L. and T.P.; funding acquisition, T.P.; resources, T.P.; supervision, T.P.

REFERENCES

Al Nabhani, Z., Dulauroy, S., Marques, R., Cousu, C., Al Bounny, S., Déjardin, F., Sparwasser, T., Bérard, M., Cerf-Bensussan, N., and Eberl, G. (2019). A Weaning Reaction to Microbiota Is Required for Resistance to Immunopathologies in the Adult. Immunity 50, 1276–1288.

Anders, S., Pyl, P.T., and Huber, W. (2015). HTSeq–a Python framework to work with high-throughput sequencing data. Bioinformatics 31, 166–169.

Arévalo Sureda, E., Weström, B., Pierzynowski, S.G., and Prykhodko, O. (2016). Maturation of the Intestinal Epithelial Barrier in Neonatal Rats Coincides with Decreased FcRn Expression, Replacement of Vacuolated Enterocytes and Changed Blimp-1 Expression. PLoS ONE 11, e0164775.

Arike, L., Holmén-Larsson, J., and Hansson, G.C. (2017). Intestinal Muc2 mucin O-glycosylation is affected by microbiota and regulated by differential expression of glycosyltranferases. Glycobiology 27, 318–328.

Arike, L., Seiman, A., van der Post, S., Rodriguez Piñeiro, A.M., Ermund, A., Schütte, A., Bäckhed, F., Johansson, M.E.V., and Hansson, G.C. (2020). Protein Turnover in Epithelial Cells and Mucus along the Gastrointestinal Tract Is Coordinated by the Spatial Location and Microbiota. Cell Rep. 30, 1077–1087.

Ashburner, M., Ball, C.A., Blake, J.A., Botstein, D., Butler, H., Cherry, J.M., Davis, A.P., Dolinski, K., Dwight, S.S., Eppig, J.T., et al.; The Gene Ontology Consortium (2000). Gene ontology: tool for the unification of biology. Nat. Genet. 25, 25–29.

Bäckhed, F., Roswall, J., Peng, Y., Feng, Q., Jia, H., Kovatcheva-Datchary, P., Li, Y., Xia, Y., Xie, H., Zhong, H., et al. (2015). Dynamics and Stabilization of the Human Gut Microbiome during the First Year of Life. Cell Host Microbe 17, 690–703.

Blighe, K., Rana, S., and Lewis, M. (2019). EnhancedVolcano: Publication-ready volcano plots with enhanced colouring and labelin (R-Package).

Camp, J.G., Frank, C.L., Lickwar, C.R., Guturu, H., Rube, T., Wenger, A.M., Chen, J., Bejerano, G., Crawford, G.E., and Rawls, J.F. (2014). Microbiota modulate transcription in the intestinal epithelium without remodeling the accessible chromatin landscape. Genome Res. 24, 1504–1516.

Carbon, S., Douglass, E., Dunn, N., Good, B., Harris, N.L., Lewis, S.E., Mungall, C.J., Basu, S., Chisholm, R.L., Dodson, R.J., et al.; The Gene Ontology Consortium (2019). The Gene Ontology Resource: 20 years and still GOing strong. Nucleic Acids Res. 47 (D1), D330–D338.

Cash, H.L. (2006). Symbiotic Bacteria Direct Expression of an Intestinal Bactericidal Lectin. Science 313, 1126–1130.

Cella, M., Gamini, R., Sécca, C., Collins, P.L., Zhao, S., Peng, V., Robinette, M.L., Schettini, J., Zaitsev, K., Gordon, W., et al. (2019). Subsets of ILC3-ILC1-like cells generate a diversity spectrum of innate lymphoid cells in human mucosal tissues. Nat. Immunol. 20, 980–991.

Cheng, H., and Leblond, C.P. (1974). Origin, differentiation and renewal of the four main epithelial cell types in the mouse small intestine. V. Unitarian Theory of the origin of the four epithelial cell types. Am. J. Anat. 141, 537–561.

Clevers, H. (2013). The intestinal crypt, a prototype stem cell compartment. Cell 154, 274–284.

Cox, J., and Mann, M. (2008). MaxQuant enables high peptide identification rates, individualized p.p.b.-range mass accuracies and proteome-wide protein quantification. Nat. Biotechnol. 26, 1367–1372.

Durinck, S., Moreau, Y., Kasprzyk, A., Davis, S., De Moor, B., Brazma, A., and Huber, W. (2005). BioMart and Bioconductor: a powerful link between biological databases and microarray data analysis. Bioinformatics 21, 3439–3440.

Ermund, A., Schütte, A., Johansson, M.E.V., Gustafsson, J.K., and Hansson, G.C. (2013). Studies of mucus in mouse stomach, small intestine, and colon. I. Gastrointestinal mucus layers have different properties depending on location as well as over the Peyer's patches. Am. J. Physiol. Gastrointest. Liver Physiol. 305, G341–G347.

Granger, B., and Baker, R.F. (1950). Electron microscope investigation of the striated border of intestinal epithelium. Anat. Rec. 107, 423–441.

Grizotte-Lake, M., Zhong, G., Duncan, K., Kirkwood, J., Iyer, N., Smolenski, I., Isoherranen, N., and Vaishnava, S. (2018). Commensals Suppress Intestinal Epithelial Cell Retinoic Acid Synthesis to Regulate Interleukin-22 Activity and Prevent Microbial Dysbiosis. Immunity 49, 1103–1115.

Gronke, K., Hernández, P.P., Zimmermann, J., Klose, C.S.N., Kofoed-Branzk, M., Guendel, F., Witkowski, M., Tizian, C., Amann, L., Schumacher, F., et al. (2019). Interleukin-22 protects intestinal stem cells against genotoxic stress. Nature 566, 249–253.

Gum, J.R., Jr., Crawley, S.C., Hicks, J.W., Szymkowski, D.E., and Kim, Y.S. (2002). MUC17, a novel membrane-tethered mucin. Biochem. Biophys. Res. Commun. 291, 466–475.

Hanash, A.M., Dudakov, J.A., Hua, G., O'Connor, M.H., Young, L.F., Singer, N.V., West, M.L., Jenq, R.R., Holland, A.M., Kappel, L.W., et al. (2012). Interleukin-22 protects intestinal stem cells from immune-mediated tissue damage and regulates sensitivity to graft versus host disease. Immunity 37, 339–350.

Helander, H.F., and Fändriks, L. (2014). Surface area of the digestive tract - revisited. Scand. J. Gastroenterol. 49, 681–689.

Ito, S. (1969). Structure and function of the glycocalyx. Fed. Proc. 28, 12–25.

Johansson, M.E.V., Phillipson, M., Petersson, J., Velcich, A., Holm, L., and Hansson, G.C. (2008). The inner of the two Muc2 mucin-dependent mucus layers in colon is devoid of bacteria. Proc. Natl. Acad. Sci. USA 105, 15064–15069.

Johansson, M.E.V., Jakobsson, H.E., Holmén-Larsson, J., Schütte, A., Ermund, A., Rodríguez-Piñeiro, A.M., Arike, L., Wising, C., Svensson, F., Bäckhed, F., and Hansson, G.C. (2015). Normalization of host intestinal mucus layers requires long-term microbial colonization. Cell Host Microbe 18, 582–592.

Jostins, L., Ripke, S., Weersma, R.K., Duerr, R.H., McGovern, D.P., Hui, K.Y., Lee, J.C., Schumm, L.P., Sharma, Y., Anderson, C.A., et al.; International IBD Genetics Consortium (IIBDGC) (2012). Host-microbe interactions have shaped the genetic architecture of inflammatory bowel disease. Nature 491, 119–124.

Koenig, J.E., Spor, A., Scalfone, N., Fricker, A.D., Stombaugh, J., Knight, R., Angenent, L.T., and Ley, R.E. (2011). Succession of microbial consortia in the developing infant gut microbiome. Proc. Natl. Acad. Sci. USA 108 (Suppl 1), 4578–4585.

Kole, A., and Maloy, K.J. (2014). Control of Intestinal Inflammation by Interleukin-10. Curr. Top. Microbiol. Immunol. 380, 19–38.

Kominsky, D.J., Campbell, E.L., Ehrentraut, S.F., Wilson, K.E., Kelly, C.J., Glover, L.E., Collins, C.B., Bayless, A.J., Saeedi, B., Dobrinskikh, E., et al. (2014). IFN-γ-mediated induction of an apical IL-10 receptor on polarized intestinal epithelia. J. Immunol. 192, 1267–1276.

Krebs, H.A., and Henseleit, K. (1932). Untersuchungen uber die Harnstoffbildung im Tierkörper. Hoppe Seylers Z. Physiol. Chem. 210, 33–66.

Kühn, R., Löhler, J., Rennick, D., Rajewsky, K., and Müller, W. (1993). Interleukin-10-deficient mice develop chronic enterocolitis. Cell 75, 263–274.

Lamas, B., Richard, M.L., Leducq, V., Pham, H.-P., Michel, M.-L., Da Costa, G., Bridonneau, C., Jegou, S., Hoffmann, T.W., Natividad, J.M., et al. (2016). CARD9 impacts colitis by altering gut microbiota metabolism of tryptophan into aryl hydrocarbon receptor ligands. Nat. Med. 22, 598–605.

Love, M.I., Huber, W., and Anders, S. (2014). Moderated estimation of fold change and dispersion for RNA-seq data with DESeq2. Genome Biol. 15, 550.

Macao, B., Johansson, D.G., Hansson, G.C., and Härd, T. (2006). Autoproteolysis coupled to protein folding in the SEA domain of the membrane-bound MUC1 mucin. Nat. Struct. Mol. Biol. 13, 71–76.

Malmberg, E.K., Noaksson, K.A., Phillipson, M., Johansson, M.E.V., Hinojosa-Kurtzberg, M., Holm, L., Gendler, S.J., and Hansson, G.C. (2006). Increased levels of mucins in the cystic fibrosis mouse small intestine, and modulator effects of the Muc1 mucin expression. Am. J. Physiol. Gastrointest. Liver Physiol. 291, G203–G210.

Malmberg, E.K., Pelaseyed, T., Petersson, Å.C., Seidler, U.E., De Jonge, H., Riordan, J.R., and Hansson, G.C. (2008). The C-terminus of the transmembrane mucin MUC17 binds to the scaffold protein PDZK1 that stably localizes it to the enterocyte apical membrane in the small intestine. Biochem. J. 410, 283–289.

Manders, E.M.M., Verbeek, F.J., and Aten, J.A. (1993). Measurement of co-localization of objects in dual-colour confocal images. J. Microsc. 169, 375–382.

Mao, K., Baptista, A.P., Tamoutounour, S., Zhuang, L., Bouladoux, N., Martins, A.J., Huang, Y., Gerner, M.Y., Belkaid, Y., and Germain, R.N. (2018). Innate and adaptive lymphocytes sequentially shape the gut microbiota and lipid metabolism. Nature 554, 255–259.

Ménard, S., Förster, V., Lotz, M., Gütle, D., Duerr, C.U., Gallo, R.L., Henriques-Normark, B., Pütsep, K., Andersson, M., Glocker, E.O., and Hornef, M.W. (2008). Developmental switch of intestinal antimicrobial peptide expression. J. Exp. Med. 205, 183–193.

Mi, H., Muruganujan, A., Ebert, D., Huang, X., and Thomas, P.D. (2019). PANTHER version 14: more genomes, a new PANTHER GO-slim and improvements in enrichment analysis tools. Nucleic Acids Res. 47 (D1), D419–D426.

Middendorp, S., Schneeberger, K., Wiegerinck, C.L., Mokry, M., Akkerman, R.D.L., van Wijngaarden, S., Clevers, H., and Nieuwenhuis, E.E.S. (2014). Adult stem cells in the small intestine are intrinsically programmed with their location-specific function. Stem Cells 32, 1083–1091.

Mizuno, S., Mikami, Y., Kamada, N., Handa, T., Hayashi, A., Sato, T., Matsuoka, K., Matano, M., Ohta, Y., Sugita, A., et al. (2014). Cross-talk between RORγt+ innate lymphoid cells and intestinal macrophages induces mucosal IL-22 production in Crohn's disease. Inflamm. Bowel Dis. 20, 1426–1434.

Neu, B., Wenby, R., and Meiselman, H.J. (2008). Effects of dextran molecular weight on red blood cell aggregation. Biophys. J. 95, 3059–3065.

Olson, F.J., Bäckström, M., Karlsson, H., Burchell, J., and Hansson, G.C. (2005). A MUC1 tandem repeat reporter protein produced in CHO-K1 cells has sialylated core 1 O-glycans and becomes more densely glycosylated if coexpressed with polypeptide-GalNAc-T4 transferase. Glycobiology 15, 177–191.

Pelaseyed, T., and Bretscher, A. (2018). Regulation of actin-based apical structures on epithelial cells. J. Cell Sci. 131, jcs221853.

Pelaseyed, T., and Hansson, G.C. (2020). Membrane mucins of the intestine at a glance. J. Cell Sci. 133, jcs240929.

Pelaseyed, T., Gustafsson, J.K., Gustafsson, I.J., Ermund, A., and Hansson, G.C. (2013a). Carbachol-induced MUC17 endocytosis is concomitant with NHE3 internalization and CFTR membrane recruitment in enterocytes. Am. J. Physiol. Cell Physiol. 305, C457–C467.

Pelaseyed, T., Zäch, M., Petersson, Å.C., Svensson, F., Johansson, D.G.A., and Hansson, G.C. (2013b). Unfolding dynamics of the mucin SEA domain probed by force spectroscopy suggest that it acts as a cell-protective device. FEBS J. 280, 1491–1501.

Pelaseyed, T., Viswanatha, R., Sauvanet, C., Filter, J.J., Goldberg, M.L., and Bretscher, A. (2017). Ezrin activation by LOK phosphorylation involves a PIP$_2$-dependent wedge mechanism. eLife 6, 35437–35451.

Perez-Riverol, Y., Csordas, A., Bai, J., Bernal-Llinares, M., Hewapathirana, S., Kundu, D.J., Inuganti, A., Griss, J., Mayer, G., Eisenacher, M., et al. (2019). The PRIDE database and related tools and resources in 2019: improving support for quantification data. Nucleic Acids Res. 47 (D1), D442–D450.

Price, A.E., Shamardani, K., Lugo, K.A., Deguine, J., Roberts, A.W., Lee, B.L., and Barton, G.M. (2018). A Map of Toll-like Receptor Expression in the Intestinal Epithelium Reveals Distinct Spatial, Cell Type-Specific, and Temporal Patterns. Immunity 49, 560–575.

Rappsilber, J., Mann, M., and Ishihama, Y. (2007). Protocol for micro-purification, enrichment, pre-fractionation and storage of peptides for proteomics using StageTips. Nat. Protoc. 2, 1896–1906.

Roth, J. (1987). Subcellular organization of glycosylation in mammalian cells. Biochim. Biophys. Acta 906, 405–436.

Sato, T., Vries, R.G., Snippert, H.J., van de Wetering, M., Barker, N., Stange, D.E., van Es, J.H., Abo, A., Kujala, P., Peters, P.J., and Clevers, H. (2009). Single Lgr5 stem cells build crypt-villus structures in vitro without a mesenchymal niche. Nature 459, 262–265.

Satoh-Takayama, N., Vosshenrich, C.A.J., Lesjean-Pottier, S., Sawa, S., Lochner, M., Rattis, F., Mention, J.J., Thiam, K., Cerf-Bensussan, N., Mandelboim, O., et al. (2008). Microbial flora drives interleukin 22 production in intestinal NKp46+ cells that provide innate mucosal immune defense. Immunity 29, 958–970.

Savage, A.K., Liang, H.-E., and Locksley, R.M. (2017). The Development of Steady-State Activation Hubs between Adult LTi ILC3s and Primed Macrophages in Small Intestine. J. Immunol. 199, 1912–1922.

Sawa, S., Cherrier, M., Lochner, M., Satoh-Takayama, N., Fehling, H.J., Langa, F., Di Santo, J.P., and Eberl, G. (2010). Lineage Relationship Analysis of RORγine Innate Lymphoid Cells. Science 330, 665–669.

Schmieder, R., and Edwards, R. (2011). Quality control and preprocessing of metagenomic datasets. Bioinformatics *27*, 863–864.

Schneider, H., Berger, E., Dolan, B., Martinez-Abad, B., Arike, L., Pelaseyed, T., and Hansson, G.C. (2019). The human transmembrane mucin MUC17 responds to TNFα by increased presentation at the plasma membrane. Biochem. J. *476*, 2281–2295.

Silverberg, M.S., Cho, J.H., Rioux, J.D., McGovern, D.P.B.B., Wu, J., Annese, V., Achkar, J.-P.P., Goyette, P., Scott, R., Xu, W., et al. (2009). Ulcerative colitis-risk loci on chromosomes 1p36 and 12q15 found by genome-wide association study. Nat. Genet. *41*, 216–220.

Sonnenberg, G.F., Monticelli, L.A., Alenghat, T., Fung, T.C., Hutnick, N.A., Kunisawa, J., Shibata, N., Grunberg, S., Sinha, R., Zahm, A.M., et al. (2012). Innate Lymphoid Cells Promote Anatomical Containment of Lymphoid-Resident Commensal Bacteria. Science *336*, 1321–1325.

Supek, F., Bošnjak, M., Škunca, N., and Šmuc, T. (2011). REVIGO summarizes and visualizes long lists of gene ontology terms. PLoS ONE *6*, e21800.

Takashima, S., Martin, M.L., Jansen, S.A., Fu, Y., Bos, J., Chandra, D., O'Connor, M.H., Mertelsmann, A.M., Vinci, P., Kuttiyara, J., et al. (2019). T cell-derived interferon-γ programs stem cell death in immune-mediated intestinal damage. Sci. Immunol. *4*, eaay8556.

Tinevez, J.-Y., Perry, N., Schindelin, J., Hoopes, G.M., Reynolds, G.D., Laplantine, E., Bednarek, S.Y., Shorte, S.L., and Eliceiri, K.W. (2017). TrackMate: An open and extensible platform for single-particle tracking. Methods *115*, 80–90.

Vonarbourg, C., Mortha, A., Bui, V.L., Hernandez, P.P., Kiss, E.A., Hoyler, T., Flach, M., Bengsch, B., Thimme, R., Hölscher, C., et al. (2010). Regulated expression of nuclear receptor RORγt confers distinct functional fates to NK cell receptor-expressing RORγt(+) innate lymphocytes. Immunity *33*, 736–751.

Walsh, M.D., Young, J.P., Leggett, B.A., Williams, S.H., Jass, J.R., and McGuckin, M.A. (2007). The MUC13 cell surface mucin is highly expressed by human colorectal carcinomas. Hum. Pathol. *38*, 883–892.

Wang, Y.-C., Li, S., Chen, X., Ma, B., He, H., Liu, T., Yu, J., Zhang, L., Chen, Y., Liu, Z., and Li, W. (2016). Meibomian Gland Absence Related Dry Eye in Ectodysplasin A Mutant Mice. Am. J. Pathol. *186*, 32–42.

Wang, L., Wu, Y., Zhuang, L., Chen, X., Min, H., Song, S., Liang, Q., Li, A.-D., and Gao, Q. (2019). Puerarin prevents high-fat diet-induced obesity by enriching Akkermansia muciniphila in the gut microbiota of mice. PLoS ONE *14*, e0218490.

Wiśniewski, J.R., Zougman, A., Nagaraj, N., and Mann, M. (2009). Universal sample preparation method for proteome analysis. Nat. Methods *6*, 359–362.

Wolk, K., Witte, E., Hoffmann, U., Doecke, W.-D., Endesfelder, S., Asadullah, K., Sterry, W., Volk, H.-D., Wittig, B.M., and Sabat, R. (2007). IL-22 induces lipopolysaccharide-binding protein in hepatocytes: a potential systemic role of IL-22 in Crohn's disease. J. Immunol. *178*, 5973–5981.

Zheng, Y., Valdez, P.A., Danilenko, D.M., Hu, Y., Sa, S.M., Gong, Q., Abbas, A.R., Modrusan, Z., Ghilardi, N., de Sauvage, F.J., and Ouyang, W. (2008). Interleukin-22 mediates early host defense against attaching and effacing bacterial pathogens. Nat. Med. *14*, 282–289.

STAR★METHODS

KEY RESOURCES TABLE

REAGENT or RESOURCE	SOURCE	IDENTIFIER
Antibodies		
Rabbit anti-Muc13 polyclonal antibody against human and mouse MUC13	(Walsh et al., 2007)	N/A
Rabbit anti-MUC17C1 polyclonal antibody against human MUC17	(Schneider et al., 2019)	N/A
Rabbit anti-Muc17S2 polyclonal antibody against mouse Muc17	(Malmberg et al., 2006)	N/A
Rabbit anti-Muc17C1 polyclonal antibody against mouse Muc17	(Malmberg et al., 2006)	N/A
Anti-Actin C4 monoclonal antibody	Millipore	RRID: AB_2223041
Mouse anti-Ezrin monoclonal antibody	Sigma-Aldrich	RRID: AB_476955
Rat anti-Il22ra1 polyclonal antibody	R&D Systems	RRID: AB_1857199
Rabbit anti-Lysozyme polyclonal antibody	Genway Biotech	RRID: AB_10528813
Rabbit anti-Muc2 polyclonal antibody	GeneTex Inc.	RRID: AB_1950958
Mouse anti-Villin monoclonal antibody	Santa Cruz	RRID: AB_2304475
Goat anti-mouse IgG1 Alexa Fluor 555	ThermoFisher Scientific	RRID: AB_2535769
Goat anti-rabbit Alexa Fluor 647	ThermoFisher Scientific	RRID: AB_2535813
Donkey anti-rabbit IgG Alexa Fluor 488	ThermoFisher Scientific	RRID: AB_2535792
Donkey anti-mouse Alexa Fluor 680	ThermoFisher Scientific	RRID: AB_2534014
Goat anti-rabbit Alexa Fluor 790	ThermoFisher Scientific	RRID: AB_2534142
Bacterial and virus strains		
E. coli DH12α	GIBCO BRL, Life Technologies, USA	N/A
Chemicals, peptides, and recombinant proteins		
Mouse EGF Recombinant Protein	GIBCO	PMG8041
R-spondin 1	Peprotech	315-32
Noggin	Sigma-Aldrich	SRP3227
MPLAs	InvivoGen	tlrl-mpls
rIl10	R&D Systems	417-ML
rIl22	R&D Systems	582-ML
Flagellin	Invivogen	tlrl-pbsfla
Ultrapure LPS from *Escherichia coli* 0111:B4	Invivogen	tlrl-3pelps
P3CSK4	Invivogen	tlrl-pms
Poly(I:C) (HMW)	Invivogen	tlrl-pic
5-Ethynyl-2′-deoxyuridine	Sigma-Aldrich	900584
Alexa Fluor 488 Azide	ThermoFisher Scientific	A10266
Lipofectamine 2000	ThermoFisher Scientific	11668019
G418 sulfate	ThermoFisher Scientific	10131035
Matrigel (growth factor-reduced)	Corning	354230
Serum free Advanced/DMEM-F12	GIBCO	12634010
N2 supplement	GIBCO	17502001
B27 supplement	GIBCO	17504044
HyClone IMDM Modified medium	Cytiva	SH30228.01
Fetal Bovine Serum	ThermoFisher Scientific	10270106
CDM-HD	Fiber Cell Systems	CDM-HD

(Continued on next page)

Continued

REAGENT or RESOURCE	SOURCE	IDENTIFIER
Ni Sepharose 6 Fast Flow	Cytiva	17531802
Mini S 4.6/50 PE	Cytiva	17517801
CellMask Deep Red plasma membrane	ThermoFisher Scientific	C10046
Fixable anionic fluorescent dextran conjugate 2,000 kDa	ThermoFisher Scientific	D7137
Ruthenium Red	SigmaAldrich	R2751
EDTA-free Complete protease inhibitor cocktail	Roche	34044100
PMSF	Sigma-Aldrich	78830
4-12% SDS-polyacrylamide	ThermoFisher Scientific	XP04125BOX
Imperial Protein Stain	ThermoFisher Scientific	24615
PVDF-FL membrane	Millipore	05317
RNAlater	QIAGEN	76104
RNeasy Plus Mini Kit	QIAGEN	74134
DNase Max Kit	QIAGEN	15200-50
High-Capacity cDNA Reverse Transcription Kit	ThermoFisher Scientific	4368814
SsoFastTM EvaGreen® Supermix	Bio-Rad	1725200
SsoAdvanced Universal Probes Supermix	Bio-Rad	1725280
10 kDa cutoff filters	PALL	OD010C33
Reprosil-Pur C18-AQ 3 mm particles	Dr. Maisch In-house packed	In-house packed
StageTip C18 columns	(Rappsilber et al., 2007)	In-house packed
Critical commercial assays		
HEK Blue Detection	InvivoGen	hb-det2
Deposited data		
RNA-sequencing analysis of mouse ileum	This paper	GEO: GSE164552
Proteomic analysis of IECs isolated from mouse ileum	This paper	ProteomeXchange: PXD018592
Raw data from Figures 1, 3, 4, 5, 6, 7, S4, and S5	Mendeley Data	https://dx.doi.org/10.17632/g6wp3mbwwz.1
Experimental models: cell lines		
HEK-Blue mTLR4 Reporter cells	InvivoGen	hkb-mtlr4
HEK-Blue Null2 Reporter cells	InvivoGen	hkb-null2
CHO-K1	ATCC	CCL-61
Experimental models: organisms/strains		
Mouse: C57BL/6N	Taconic	B6
Oligonucleotides		
qRT-PCR: *Muc17* Forward: GCCGTGAATTGTATGAACGGA	Eurofins Genomics	Mouse *Muc17* (NM_010843.1)
qRT-PCR: *Muc17* Reverse: CGCAGTTGACCACGTTGACTA	Eurofins Genomics	Mouse *Muc17* (NM_010843.1)
qRT-PCR: *Muc13* Forward: TTTGGCTACAGCGGGATGAA	(Wang et al., 2016)	Mouse *Muc13* (NM_010739.2)
qRT-PCR: *Muc13* Reverse: AGATGAGGATGAGGGCTCCA	(Wang et al., 2016)	Mouse *Muc13* (NM_010739.2)
qRT-PCR: *Reg3g* Forward: ATGCTTCCCCGTATAACCATCA	(Wang et al., 2019)	Mouse *Reg3g* (NM_011260.2)
qRT-PCR: *Reg3g* Reverse: ACTTCACCTTGCACCTGAGAA	(Wang et al., 2019)	Mouse *Reg3g* (NM_011260.2)

Continued

REAGENT or RESOURCE	SOURCE	IDENTIFIER
qRT-PCR: *Gapdh* Forward: GGAGAAACCTGCCAAGTATG	(Johansson et al., 2015)	Mouse *Gapdh* (NM_008084.3)
qRT-PCR: *Gapdh* Reverse: GGAGTTGCTGTTGAAGTCG	(Johansson et al., 2015)	Mouse *Gapdh* (NM_008084.3)
qRT-PCR: *β-actin* Forward: AACGAGCGGTTCCGATGC	(Johansson et al., 2015)	Mouse *β-actin* (NM_007393.5)
qRT-PCR: *β-actin* Reverse: GTAGTTTCATGGATGCCACAGG	(Johansson et al., 2015)	Mouse *β-actin* (NM_007393.5)
Mouse *Il22*	Bio-Rad	qMmuCEP0060632
Mouse *Gapdh*	Bio-Rad	qMmuCEP0039581
Mouse *β-actin*	Bio-Rad	qMmuCEP0039589
Recombinant DNA		
Mouse recombinant Il22bp in pcDNA3.1(+)-C-6His	GenScript	OMu07196 (NM_178258.5)
pGFPuv	Takara	632312
Software and algorithms		
ImageJ	NIH	Version 2.1.0/1.53c
RStudio	RStudio, Inc.	Version 1.2.5033
TrackMate	(Tinevez et al., 2017)	Version 4.0.0.
Coloc 2	ImageJ	Version 3.0.0
FastQC	Babraham Bioinformatics	Version 0.11.2
prinseq	(Schmieder and Edwards, 2011)	Version 0.20.3
HTseq	(Anders et al., 2015)	Version 0.6.1p1
TPM	(Durinck et al., 2005)	N/A
DESeq2	(Love et al., 2014)	Version 1.14
EnhancedVolcano	(Blighe et al., 2019)	N/A
Gene ontology enrichment analysis	(Ashburner et al., 2000; Carbon et al., 2019; Mi et al., 2019);	Release 2020-11-17
REVIGO	(Supek et al., 2011)	N/A
Other		
MaxQuant	(Cox and Mann, 2008)	Version 1.5.7.4
Mouse protein database	UniProt	Downloaded 2018.07.11
Mouse mucin sequences	Mucin Biology Groups University of Gothenburg	http://www.medkem.gu.se/mucinbiology/databases/

RESOURCE AVAILABILITY

Lead contact
Further information and requests for resources and reagents should be directed to and will be fulfilled by the lead contact, Thaher Pelaseyed (thaher.pelaseyed@medkem.gu.se).

Materials availability
This study did not generate new unique reagents.

Data and code availability
All datasets associated with this study are available on the public repositories NCBI Gene Expression Omnibus (RNA-seq, GEO: GSE164552) and ProteomeXchange Consortium (proteomics, ProteomeXchange: PDX018592). Raw data from Figures 1, 3, 4, 5, 6, 7, S4, and S5 has been deposited to Mendeley at https://dx.doi.org/10.17632/g6wp3mbwwz.1.

EXPERIMENTAL MODEL AND SUBJECT DETAILS

Human subjects

Human biopsies were collected from ileum of individuals without suspected Inflammatory Bowel Disease (IBD), who were referred to Sahlgrenska University Hospital (Gothenburg, Sweden) for colonoscopy, and subject to the provision of written informed consent (ethical permit 136-12). Ileal sections for immunohistochemistry were obtained from a 37 year old female.

Mice

Wild-type (WT) C57BL/6N mice were maintained under standardized conditions of temperature (21–22°C) and illumination (12-hour light/dark cycle) with food and water *ad libitum*. The Swedish Laboratory Animal Ethical Committee in Gothenburg approved the experiments carried out in this study (Ethical permits 73-15 and 2285-19). The care and use of animals were performed in accordance with the Swedish animal welfare legislation, which meets the European Convention for the Protection of Vertebrate Animals used for Experimental and other Scientific Purposes (Council of Europe No 123, Strasbourg 1985) and the European Union Directive 2010/63/EU on the protection of animals used for scientific purposes. Animals were anesthetized with isoflurane followed by cervical dislocation. Animals of 9 days old (P9) to 6 weeks of age and of both genders were used. Weaning occurred on day 21 after birth (P21).

Mouse ileal organoids

Crypts were released from small intestinal tissue of adult WT C57BL/6N mouse and organoids were generated as described previously (Sato et al., 2009). Briefly, crypts were released from murine ileal tissue following incubation in ice cold PBS containing 5 mM EDTA. Isolated crypts were pelleted by centrifugation, mixed with growth factor-reduced Matrigel (#354230, Corning) and plated in 24-well cell culture plates. Cultures were maintained in serum free Advanced/DMEM-F12 (#12634010, GIBCO) supplemented with 1x N2 supplement (#17502001, GIBCO), 1x B27 supplement (#17504044, GIBCO), 50 ng/ml EGF (#PMG8041, GIBCO), 500 ng/ml R-spondin 1 (#315-32, Peprotech) and 100 ng/ml Noggin (#SRP3227, Sigma-Aldrich) and incubated in a humidified atmosphere containing 5% CO_2 at 37°C. Medium was replaced every second day and organoids were passaged by mechanical fragmentation into crypt domains followed by seeding in fresh Matrigel. For experiments, organoids were seeded and maintained for 6 days before use.

Cell lines

CHO-K1 (#CCL-61, ATCC) were maintained in a 5% CO_2 humidified atmosphere at 37°C, in HyClone IMDM Modified medium (#SH30228.01, Cytiva) supplemented with 10% fetal bovine serum (#10270106, ThermoFisher Scientific) or 2% CDM-HD (#CDM-HD, Fiber Cell Systems).

Bacteria

DH12α strain (GIBCO BRL, Life Technologies, USA) was cultured overnight at 37°C in LB medium (100 μg/mL ampicillin).

METHOD DETAILS

Determination of physiological concentration of LPS in mouse ileum

In vivo concentrations of LPS in mouse ileum were determined using HEK-Blue TLR Reporter cells (mTLR4 #hkb-mtlr4 and Null2 #hkb null2, InvivoGen). HEK-Blue mTLR4 and parental Null2 cells were resuspended in HEK Blue Detection (#hb-det2, InvivoGen). 25,000 cells/well of each reporter line were added to 96-well plates containing synthetic *E. coli* Lipid A analog MPLAs (1×10^6 endotoxin units (EU)/mg) concentration standard (#tlrl-mpls, InvivoGen) or serial dilutions of 100 mg/mL homogenized ileum of P14 or P24 mice in sterile, endotoxin-free PBS. After 16 hr of incubation in a humidified atmosphere containing 5% CO_2 at 37°C, mTLR4-induced secreted embryonic alkaline phosphatase (SEAP) activity was detected at 655 nm using a Spectramax M2e (Molecular Devices) microplate reader. SEAP activity in mouse ileum was converted to EU/mL.

Stimulation of organoids and intestinal epithelial cells

Organoids were retrieved using Cell recovery solution (#354253, Corning), washed in PBS and resuspended in organoid culture medium described in "Organoid cultures." For isolation of IECs, mesenteric tissue was removed and the ileum was cut longitudinally and incubated in PBS containing 3 mM EDTA and 1 mM DTT at 37°C for 60 min. The solution was replaced with fresh 37°C PBS and epithelial cells were dissociated from the tissue by vigorous shaking for 5 × 20 s. Remaining tissue was removed and cells were pelleted by centrifugation at 1000 g for 5 min. IECs were washed with PBS and resuspended in HyClone Iscove's Modified Dulbecco's Medium + 10% (vol/vol) fetal calf serum. Organoids or isolated IECs were stimulated with of 50 ng/mL rIl10 (#417-ML, R&D Systems), 50 ng/mL rIl22 (#582-ML, R&D Systems), 100 ng/mL Flagellin (#tlrl-pbsfla, Invivogen), 25-140 EU/mL ultrapure LPS from *Escherichia coli* 0111:B4 (#tlrl-3pelps, Invivogen), 1 μg/mL P3CSK4 (#tlrl-pms, Invivogen), or 20 μg/mL Poly(I:C) (HMW) (#tlrl-pic, Invivogen), for 4 hr in a humidified atmosphere containing 5% CO_2 at 37°C. After incubation, organoids or IECs were prepared for downstream qRT-PCR analysis.

In vivo treatment of mice with Il22 and 5-Ethynyl-2′-deoxyuridine (EdU)

Mice at postnatal day 14 (P14) were treated with two intraperitoneal (i.p.) doses (0.1 μg/g bodyweight) of rIl22 or PBS with a 24 h interval. Three animals were sacrificed at P16, corresponding to 24 hr after last injection. For the spatiotemporal expression of Muc17 in response to rIl22 *in vivo*, P14 mice were i.p injected with a combined treatment of 0.2 μg/g bodyweight of rIl22 and 1 mM/g bodyweight of 5-Ethynyl-2′-deoxyuridine (EdU) (#900584, Sigma-Aldrich). Three animals were sacrificed 2, 24 and 48 hr after i.p. injection. For pulse-chase tracking of cells during the suckling-weaning transition, 1 mM/g bodyweight of EdU was i.p. injected to P16 animals. Three animals were sacrificed 2, 24, 48, 72 and 96 hr after i.p. injection.

Production of recombinant IL-22 binding protein and intraperitoneal injection

Mouse recombinant (r)Il22bp (NM_178258.5) was cloned into pcDNA3.1(+)-C-6His using HpaI and *XbaI* restriction sites. CHO-K1 (#CCL-61, ATCC) cells were transfected using Lipofectamine 2000 (#11668019, Thermo Scientific) and stable clones were selected using 800 μg/mL G418 sulfate (#10131035, Thermo Scientific). rIl22bp-6His was collected for 48 hr into HyClone IMDM Modified medium (#SH30228.01, Cytiva) supplemented with 2% CDM-HD (#CDM-HD, Fiber Cell Systems). Spent medium was dialyzed against 20 mM sodium phosphate, 500 mM NaCl, pH 7.3. 2 mL Ni Sepharose 6 Fast Flow (#17531802, Cytiva) was equilibrated with 10 CV Wash buffer (20 mM sodium phosphate, 500 mM NaCl, 40 mM Imidazole, pH 7.3), spent medium was run over Ni Sepharose and column was washed with 20 CV Wash buffer. rIl22bp was eluted in 0.5 mL fractions with 5 CV Elution buffer (20 mM sodium phosphate, 500 mM NaCl, 500 mM Imidazole, pH 7.3) (See Figure S5C). Fractions containing rIl22bp were dialyzed against Buffer A (20 mM Tris-HCl, 40 mM NaCl, pH 7.0) and purified on Mini S 4.6/50 PE (#17517801, Cytiva) cation exchange column using a gradient of Buffer B (20 mM Tris buffer 500 mM NaCl, pH 7.0) (40 mM - 500 mM NaCl, 20 CV) (See Figure S5C). Pure rIl22bp fractions were dialyzed against PBS. 50 μg of rIl22bp in 100 μL PBS was administered through intraperitoneal injection at P14, P16 and P18. Tissues were collected for analysis at P20.

Tissue and organoid fixation, immunostain, AB-PAS stain and microscopy

Harvested ileum was fixed in Carnoy's fixative (60% absolute methanol, 30% chloroform and 10% glacial acetic acid) or 4% paraformaldehyde (PFA) solution. Samples fixed in Carnoy's fixative were embedded in paraffin, while PFA-fixed tissues were emerged in 30% sucrose overnight. PFA-Sucrose samples were covered with Optimal Cutting Temperature (OCT) reagent and frozen for cryosectioning. 4-10 μm sections were cut and placed on positively charged glass slides. Paraffin-embedded sections were deparaffinized in xylene substitute (2 × 10 min, 60°C) and rehydrated in 100% ethanol (10 min), 70% (v/v) ethanol (5 min), 50% (v/v) ethanol (5 min), and 30% (v/v) ethanol (5 min). Sections were placed in antigen retrieval buffer (0.01M citric acid, pH 6.0) at 100 degrees for 10 min and then brought to RT (2 hr) and transferred to PBS. Tissues were enclosed with a PAP pen followed by Click reaction and/or blocked with 5% fetal calve serum (FCS) in PBS for 2 h at room temperature (RT). Click reactions were performed by adding 8 μM Alexa Fluor 488 Azide (#A10266, Thermo Scientific) 2mM CuSO4·5H2O and 20mg/mL Ascorbic acid for 30 min followed by three PBS washes.

Primary and secondary antibodies were added in dilution buffer (5% FCS and 0.1% Triton X-100). Primary antibodies were mouse anti-Actin C4 monoclonal antibody (1:10,000) (RRID: AB_2223041, #MAB1501, Millipore), mouse anti-Ezrin monoclonal antibody (1:500) (RRID: AB_476955, #E8897, Sigma-Aldrich), rat anti-Il22ra1 polyclonal antibody (1:100) (RRID: AB_1857199, #MAB42941, R&D Systems), rabbit anti-Lysozyme polyclonal antibody (1:500) (RRID: AB_10528813, #GWB-635D48, Genway Biotech), rabbit anti-Muc2 polyclonal antibody (1:500) (RRID: AB_1950958, #GTX100664, GeneTex Inc.), rabbit anti-Muc13 polyclonal antibody against human and mouse MUC13 (1:500) (Walsh et al., 2007), rabbit anti-MUC17C1 polyclonal antibody against human MUC17 (1:500) (Schneider et al., 2019), rabbit anti-Muc17S2 polyclonal antibody against mouse Muc17 (1:2,000) (Malmberg et al., 2006), mouse anti-Villin monoclonal antibody (1:50) (RRID: AB_2304475, #sc-58897, Santa Cruz). Secondary antibodies were donkey anti-rabbit IgG Alexa Fluor 488 (1:500) (RRID: AB_2535792, #A21206, ThermoFisher Scientific), goat anti-mouse IgG1 Alexa Fluor 555 (1:500) (RRID: AB_2535769, #A21127, ThermoFisher Scientific) and goat anti-rabbit Alexa Fluor 647 (1:500) (RRID: AB_2535813, #A21245, ThermoFisher Scientific). DNA was stained with Hoechst 34580 (1:10,000) (#H21486, ThermoFisher Scientific). Coverslips were mounted using Prolong Gold antifade (#P36980, ThermoFisher Scientific) and polymerized for 2 hr at RT.

Organoids were retrieved using Cell recovery solution (#354253, Corning), washed in PBS and fixed in 4% PFA solution. Organoids were washed in PBS +1% Triton X-100 and permeabilized for 1 hr in PBS +1% Triton X-100. Organoids were washed gently in PBS and blocked for 1 hr in 5% FCS in PBS + 0.2% Triton X-100. Organoids were incubated with primary antibodies in PBS + 0.2% Triton X-100 on 5-7 rpm rotation overnight at 4°C. The next day, organoids were washed and incubated with secondary antibodies in PBS + 0.2% Triton X-100 on 5-7 rpm rotation overnight at 4°C. Finally, nuclei were stained with Hoechst for 5 min at RT. After multiple washes with PBS, organoids were mounted on coverslips.

Samples were acquired with an upright LSM 700 Axio Examiner Z.1 confocal imaging system (Carl Zeiss). AB-PAS stain was performed at pH 2.1-2.5.

Semiquantitative image analysis

Semiquantitative analysis of Muc17 expression in BBM was performed by analysis of confocal images using ImageJ software. Muc17 expression was measured as Corrected total fluorescence (CTF). Integrated Density in multiple regions of interest (ROI) in BBM with an average area of 76.3 μm were recorded. CTF was calculated using the following formula:

$$CTF = Integrated\ Density - (Area\ of\ ROI \times Mean\ Fluorescence\ of\ Background)$$

Ex vivo glycocalyx permeability assay

Ileum from pre- and postweaned mice was harvested and flushed with ice-cold Krebs transport solution (Krebs and Henseleit, 1932). In order to determine glycocalyx barrier properties without interference from overlying mucus, ileal tubes were opened longitudinally, flushed again with Krebs transport solution, and mounted with the epithelial side up *in silico*n-well plates. Mounted samples were stained with 50 μg/mL CellMask Deep Red plasma membrane stain (#C10046, Thermo Fisher Scientific) for 5 min at RT, fixed with 4% PFA for 1 h at RT and washed extensively with PBS. Fixable anionic fluorescent dextran conjugate 2,000 kDa in size (200 μg/ml) (#D7137, Thermo Fisher Scientific) was diluted in PBS and added to the luminal surface of fixed whole-mount tissue. Glycocalyx permeability assay was performed 10 minutes after addition of anionic dextran, using a Plan-Apochromat × 20/1.0 DIC water objective (Zeiss) on an upright LSM 700 Axio Examiner Z.1 confocal imaging system (Carl Zeiss). Quantification of dextran permeability along the glycocalyx-microvillus axis was performed using the line tool and plot profile analysis in ImageJ software (version 2.0.0-rc-69/1.52p). Specifically, for each channel, distribution of fluorescent signal as a function of distance (μm) was aligned in relation to maximum intensity of CellMask that corresponds to microvillus compartment. Finally, minimum and maximum intensities for each channel were set to 0 and 100, respectively. 3 lines per image, 3 images per animal and 3 animals per age group were used for quantification of glycocalyx permeability.

Bacterial penetrance into the glycocalyx and brush border compartments was quantified using *E. coli*[GFP] by transforming a DH12α strain with pGFPuv (#632312, Takara). Briefly, *E. coli*[GFP] were cultured overnight at 37°C in LB medium (100 μg/mL ampicillin) and washed in PBS prior to glycocalyx permeability assay on mouse ileal explants stained will CellMask Deep Red plasma membrane stain and fixed in PFA. Explants were incubated with *E. coli*[GFP] for 20 min prior to time-lapse confocal imaging (pixel dwell time 2.41 μsec, frame time 20.39 s) for 20 cycles. Spatial *E. coli*[GFP] intensities as a function of time were extracted using TrackMate (Tinevez et al., 2017) in ImageJ software. Thresholded Manders coefficient (tM2) (Manders et al., 1993) representing co-occurrence of *E. coli*[GFP] with CellMask was quantified using Coloc 2 plugin in ImageJ. Quantification was performed on an average of 26 regions per villus, three villi per animal and four animals per age group.

Electron microscopy

Ileal sections underwent perfusion fixation with 4% glutaraldehyde, 0.15% Ruthenium Red (#R2751, SigmaAldrich) in 0.2 M sodium cacodylate for 2 hr at RT and fixed on rotation overnight at 4°C. Following extensive washes in 0.05M cacodylate buffer and 20 nM glycine, tissues were immersed in secondary fixative (4% osmium tetroxide in water, 0.2M cacodylate buffer and 0.15% Ruthenium Red) for 2 hr in the dark. After washes in 0.2 M sodium cacodylate and water, sections were dehydrated through a graded series of ethanol and acetone at 40°C for 2 min each, and infiltrated in a graded series (25%–100%) of Hard Plus resin over a period of 3 hr and left in fresh resin overnight. The samples were embedded in molds and polymerized at 60°C for 16 hr. Sections were viewed on a Talos L120C (Thermo Fisher Scientific) operated at 120kV and equipped with a 4x4k Ceta camera.

Electrophoresis and western blot

Ileal tissues were lysed on ice in Lysis buffer (25 mM Tris-HCL pH 7.4, 150 mM NaCl, 4% glycerol, 1% Triton X-100) complemented with final concentration of 1X EDTA-free Complete protease inhibitor cocktail (#34044100, Roche) and 1 mM PMSF (#78830, Sigma-Aldrich, homogenized with 10 strokes in a 1 mL Dounce glass homogenizer and centrifuged at 24,000 x g for 30 min at 4°C. Cleared supernatants were reduced in 4X reducing sample buffer (8% SDS, 400 mM Dithiothreitol) and separated on precast 4%–12% SDS-polyacrylamide gel (#XP04125BOX, ThermoFisher Scientific). For Coomassie stains, gels were stained with Imperial Protein Stain (#24615, Thermo Scientific) overnight and destained in 5% MeOH and 7% Acetic Acid, and visualized on an Odyssey CLx near-infrared fluorescence imaging system (LI-COR Biosciences). Proteins were transferred to a PVDF-FL membrane (#05317, Millipore) with a current of 2.5 mA/cm^2 for 1 h. Membrane was blocked in 5% non-fat milk in PBS for 30 min and incubated with rabbit anti-Muc17C1 polyclonal antibody against mouse Muc17 (1:250) (Malmberg et al., 2006) and anti-Actin C4 monoclonal antibody (1:4000) (RRID: AB_2223041, #MAB1501, Millipore) in 5% non-fat milk in PBS + 0.1% Tween-20 (PBS-T) overnight at 4°C. Membrane was washed three time in PBS-T and incubated with donkey anti-mouse Alexa Fluor 680 (1:20000) (RRID: AB_2534014, #A10038, ThermoFisher Scientific) and goat anti-rabbit Alexa Fluor 790 (1:20000) (RRID: AB_2534142, A11369, ThermoFisher Scientific) secondary antibodies for 1 hr at RT in the dark. Membrane was washed three time in PBS-T and visualized on an Odyssey CLx near-infrared fluorescence imaging system (LI-COR Biosciences). Protein quantification was performed using Image Studio quantification software (LI-COR Biosciences).

Quantitative RT-PCR

Ileum samples for mRNA analysis were collected in RNAlater (#76104, QIAGEN) and kept at −80°C until RNA extraction. Total RNA was isolated using RNeasy Plus Mini Kit (#74134, QIAGEN) and DNase Max Kit (#15200-50, QIAGEN), followed by storage at −80°C. Complementary DNA was synthesized for qRT-PCR by using High-Capacity cDNA Reverse Transcription Kit (#4368814, ThermoFisher Scientific). SsoFastTM EvaGreen® Supermix (#1725200, Bio-Rad) and specific primers were used to quantify mRNA expression. Mouse *Il22* transcript analysis was performed by using SsoAdvanced Universal Probes Supermix (#1725280,

Bio-Rad) and specific primers from Bio-Rad (Table S2). Reactions were run using the CFX96 Real-Time PCR Detection System (Bio-Rad). Absence of genomic DNA contamination in the RNA preparation was controlled by PCR amplification of RNA samples without previous reverse transcription. Three independent experiments were performed with each sample measured in triplicates. Transcripts were normalized to *Gapdh* and *β-actin.* mRNA expression was calculated as $\Delta\Delta Ct = \Delta Ct_{treatment} - \Delta Ct_{control}$, where $\Delta Ct = Ct_{gene} - mean(Ct_{calibrators})$. Relative gene expression was transformed and expressed as the fold change ($= 2^{-\Delta\Delta Ct}$). Gene-specific qPCR primer sequences used for detection of mRNAs are given in Tables S4 and S5.

Bulk RNA-sequencing
RNA sequencing was performed by the Genomics Core Facility at the Sahlgrenska Academy (Gothenburg, Sweden). The quality of isolated RNA was determined using a Bioanalyzer (Agilent) with RIN values greater than 8. cDNA libraries were prepared using the TruSeq Stranded Total RNA Sample Preparation kit with Ribo Zero Gold (Rev. E; Illumina) according to manufacturer's protocol, and sequenced thereafter via paired-end with the NextSeq500 platform (Illumina). The sequencing quality was measured for all lanes, reads and cycles with 93.4% of bases above Q30. Quality of raw data was assessed using FastQC (version 0.11.2) looking at per base sequence quality and adaptor contamination. If required, Fastq files were quality filtered using prinseq (version 0.20.3) (Schmieder and Edwards, 2011). The reads were mapped against the mouse reference genome mm10 from Ensembl using STAR (version 2.4.0f for the DC and 2.5.2b for the Si8). The number of mapped reads was calculated using HTseq (version 0.6.1p1) (Anders et al., 2015) with the stranded reverse protocol. Normalization for transcripts per million (TPM) was performed using "biomaRt" library in R (Durinck et al., 2005). Normalization for differential gene expression was performed using DESeq2 (version 1.14) in R (Love et al., 2014). Heatmaps were generated using "pheatmap" and "viridis" libraries in R . Volcano plots were drawn using "EnhancedVolcano" library in R (Blighe et al., 2019). Enriched biological processed were identified using Gene ontology enrichment analysis (Ashburner et al., 2000; Carbon et al., 2019; Mi et al., 2019) and condensed using REVIGO (Supek et al., 2011).

Protein extraction and digestion for mass spectrometry
Isolated epithelial cells were lysed by addition of 400 μL lysis buffer (100 mM DTT, 4% SDS, 100 mM Tris pH 7,5) and heated for 5 min at 95°C. Cell lysates were sonicated for 10 s, centrifuged at 16,000 x g in a tabletop centrifuge at RT and supernatant added onto 10 kDa cutoff filters (#OD010C33, PALL). Proteins were digested using filter-aided sample preparation (Wiśniewski et al., 2009) with trypsin at 37°C overnight. Peptide concentration after elution was measured at 280 nm using NanoDrop (Thermo Fisher Scientific) and peptides cleaned with StageTip C18 columns (Rappsilber et al., 2007) prior to mass-spectrometry (MS) analysis.

Liquid Chromatography-MS/MS
Nano LC-MS/MS was performed on a Q-Exactive HF mass-spectrometer (Thermo Fischer Scientific), connected with an EASY-nLC 1000 system (Thermo Fischer Scientific) through a nanoelectrospray ion source. Peptides were loaded on a reverse-phase column (150 mm³ 0.075 mm inner diameter, New Objective, New Objective, Woburn, MA) packed in-house with Reprosil-Pur C18-AQ 3 mm particles (Dr. Maisch, Ammerbuch, Germany). Peptides were separated with a 230-minute gradient: from 3 to 25% B in 175 min, 25 to 45% B in 30 min, 45 to 100% B in 5 min, followed 20 min wash with 100% of B (A: 0.1% formic acid, B: 0.1% formic acid/80% acetonitrile) using a flow rate of 250 nl/min. Q-Exactive HF was operated at 250°C capillary temperature and 2.0 kV spray voltage. Full mass spectra were acquired in the Orbitrap mass analyzer over a mass range from m/z 350 to 1600 with resolution of 60 000 (m/z 200) after accumulation of ions to a 3e6 target value based on predictive AGC from the previous full scan. Twelve most intense peaks with a charge state $\geq$ 2 were fragmented in the HCD collision cell with normalized collision energy of 27%, and tandem mass spectrum was acquired in the Orbitrap mass analyzer with resolution of 15 000 after accumulation of ions to a 1e5 target value. Dynamic exclusion was set to 30 s. The maximum allowed ion accumulation times were 20 ms for full MS scans and 50 ms for tandem mass spectrum.

MS data analysis
MS raw files were processed with MaxQuant software version 1.5.7.4 (Cox and Mann, 2008), peak lists were identified by searching against the mouse UniProt protein database (downloaded 2018.07.11) supplemented with an in-house database containing all the mouse mucin sequences (http://www.medkem.gu.se/mucinbiology/databases/). Searches were performed using trypsin as an enzyme, maximum 2 missed cleavages, precursor tolerance of 20 ppm in the first search used for recalibration, followed by 7 ppm for the main search and 0.5 Da for fragment ions. Carbamidomethylation of cysteine was set as a fixed modification, methionine oxidation and protein N-terminal acetylation were set as variable modifications. The required false discovery rate (FDR) was set to 1% both for peptide and protein levels and the minimum required peptide length was set to seven amino acids. Label free quantification (LFQ) based on two peptides was used. The mass spectrometry proteomics data have been deposited to the ProteomeXchange Consortium (http://proteomecentral.proteomexchange.org) via the PRIDE partner repository (Perez-Riverol et al., 2019) with the dataset identifier PXD018592. Obtained data was analyzed with Perseus (version 1.5.5.0) by removing reverse proteins and proteins only identified by site and contaminants. Intensities were transformed using a $\log_2(x)$ function and filtered based on valid values criteria (a minimum of 3 valid values in at least one of the groups). Missing values were imputed with a width of 0.3 of the Gaussian distribution relative to the standard deviation of measured values and downshift of 1.8 units of standard deviation of the valid data. Heatmaps and volcano plots were generated in R as described above.

QUANTIFICATION AND STATISTICAL ANALYSIS

Data analysis was performed using GraphPad Prism (version 8), Perseus (version 1.5.5.0) and R open source software. Graphs were prepared using GraphPad Prism (version 8). Two-tailed unpaired t test followed by Welch's correction or Mann-Whitney test were used for comparison of two groups. One-way or two-way ANOVA followed by Dunnett's or Sidak's multiple comparison test were used for comparisons of multiple groups. ns, non-significant, $*p < 0.05$, $**p < 0.01$, $*** p < 0.001$, $****p < 0.0001$.